

Excited states of van der Waals clusters by projector Monte Carlo, with application to excitations of molecules in small 4He n

D. Blume, M. Mladenović, M. Lewerenz, and K. B. Whaley

Citation: *The Journal of Chemical Physics* **110**, 5789 (1999); doi: 10.1063/1.478477

View online: <http://dx.doi.org/10.1063/1.478477>

View Table of Contents: <http://scitation.aip.org/content/aip/journal/jcp/110/12?ver=pdfcov>

Published by the [AIP Publishing](#)

Articles you may be interested in

[Interdimensional degeneracies in van der Waals clusters and quantum Monte Carlo computation of rovibrational states](#)

J. Chem. Phys. **123**, 014304 (2005); 10.1063/1.1941107

[Quantum statistical mechanics with Gaussians: Equilibrium properties of van der Waals clusters](#)

J. Chem. Phys. **121**, 9247 (2004); 10.1063/1.1804495

[Rotational dynamics of CO solvated in small He clusters: A quantum Monte Carlo study](#)

J. Chem. Phys. **120**, 9071 (2004); 10.1063/1.1697388

[van der Waals bending bands of the ArDCN cluster observed by millimeter-wave spectroscopy combined with a pulsed supersonic jet technique](#)

J. Chem. Phys. **113**, 1524 (2000); 10.1063/1.481965

[Adiabatic diffusion Monte Carlo approaches for studies of ground and excited state properties of van der Waals complexes](#)

J. Chem. Phys. **110**, 5481 (1999); 10.1063/1.478444



Excited states of van der Waals clusters by projector Monte Carlo, with application to excitations of molecules in small $^4\text{He}_n$

D. Blume

*Max-Planck-Institut für Strömungsforschung, Bunsenstr. 10, D-37073 Göttingen, Germany
and Department of Chemistry, University of California, Berkeley, California 94720*

M. Mladenović

Institut für Physikalische Chemie, Tammannstr. 6, D-37077 Göttingen, Germany

M. Lewerenz

*Max-Planck-Institut für Strömungsforschung, Bunsenstr. 10, D-37073 Göttingen, Germany
and Zentralinstitut für Angewandte Mathematik, Forschungszentrum Jülich, D-52425 Jülich, Germany*

K. B. Whaley

Department of Chemistry, University of California, Berkeley, California 94720

(Received 24 August 1998; accepted 23 December 1998)

We demonstrate the extraction of excited rovibrational state energies for quantum systems with up to 15 dimensions, using the recently developed projection operator imaginary time spectral evolution (POITSE) method. The technique is applied to a series of model van der Waals complexes of the form $AB-X_n$, $n = 1-3$, with heavy AB and a weakly bound, light atom X . The selectivity of several types of molecule-fixed and space-fixed projectors and their relationship to the nature of the accessible excited states are studied by making comparison with discrete variable-finite basis representation (DVR-FBR) calculations for $n=1$. These also allow identification of excitations dominant in ground state infrared absorptions. The results suggest a propensity for space-fixed projectors to access states where the angular momentum of the diatomic AB dominates the overall angular momentum, while molecule-fixed projectors access primarily bending and stretching modes. The relevance of this observation for the interpretation of the rovibrational spectra of molecules embedded in large liquid helium clusters is discussed. © 1999 American Institute of Physics. [S0021-9606(99)01912-1]

I. INTRODUCTION

The calculation of excited states for truly multidimensional quantum systems is a problem of continuing interest and importance in chemical physics. Quantum Monte Carlo (MC) methods offer attractive scaling with dimensionality, and thereby the possibility of circumventing the exponential growth associated with basis set methods. Quantum Monte Carlo calculations of excited states are generally performed within the fixed node approximation, requiring prior knowledge of, or, at least, good estimates of the nodal structure.^{1,2} Supplying this becomes more difficult as the number of dimensions increases. While some significant progress has been made with some released node approaches in the field of fermion problems in recent years,³ there is still no robust and general algorithm for excited states which does not require a nodal approximation.

We have recently explored an alternative approach for the direct calculation of excited states which focuses merely on the calculation of the excited state energies, rather than aiming for both energies and wave functions. By making use of recent developments in image reconstruction analysis,⁴ we showed that it is possible to extract excited state energies from the inverse Laplace transform of an imaginary time correlation function which is computed with a zero temperature diffusion Monte Carlo (DMC) algorithm.⁵⁻⁷ In its sim-

plest form, the algorithm starts with a projection from the ground state to some excited state, and the imaginary time evolution of this is then followed for some time. A subsequent inversion yields the desired spectral information. We have termed the method POITSE, or projection operator imaginary time spectral evolution, to reflect these primary features. Although the method can be applied to any bound system, initial studies of the algorithm were restricted to low dimensional test systems emulating molecular excitations involving nuclear motions. These showed the method to be versatile, allowing both vibrational and rotational excitations, and tunneling splittings to be calculated with accuracies of a few percent or less. Thus while the POITSE method does not have the well-defined convergence properties of basis set methods, and does not always yield spectroscopic accuracy, it was demonstrated to be a general method to obtain excited state energies of all kinds exact to a few percent. The polynomial growth of the computer time needed for the Monte Carlo propagation makes this method attractive for systems too large to be dealt with by conventional methods which more typically show exponential growth. For example, while basis set methods have recently been extended to allow 6-dimensional calculations,⁸⁻¹⁰ it is shown below that the POITSE method can readily extract excitations in up to 15-dimensional systems. The algorithm can also be used without further theoretical modification for much larger sys-

tems, although computational considerations will then warrant investment in a high density parallelization. Furthermore, since the method deals with energy differences rather than absolute energies, it lends itself naturally to the calculation of tunneling splittings or other small energy differences in complex spectra. These often prove impossible to extract from basis set calculations because of their small size, whereas POITSE allows calculation to within a few percent no matter what the absolute value of the energy difference. For these two reasons, while POITSE does not necessarily yield spectroscopic accuracy, it can often deliver the *spectroscopically relevant* energy differences in situations where conventional methods fail completely. Thus it is a very promising approach for further application in large clusters and molecular systems.

In this paper we apply POITSE to a larger system, addressing the excitations of van der Waals complexes of the form $AB-X_n$. In the largest instance studied here, $n=3$, this yields a 15-dimensional system of coupled atoms (nine internal degrees of freedom), well beyond the capabilities of conventional basis set methods. For the “dimer” $AB-X$, discrete variable-finite basis (DVR-FBR) calculations are performed to benchmark the POITSE results. These also afford useful insights into the nature of the excitations and their spectral accessibility, because the availability of a wave function allows a precise assignment of the accessed states. By comparing the states accessed by various choices of projectors with exact variational results for a small system, we can identify which types of projectors access which type of state, thereby allowing a fine tuning of projectors for applications to larger systems, where basis set calculations are impossible. A careful study of the influence of projectors on the selection of excited states appearing in a given POITSE spectrum is needed because POITSE provides us only with the value of the excitation energy. In particular, we are interested in identifying projectors which can selectively address excitations which are associated with molecular motion inside a larger system, in the context of recent spectroscopic experiments involving molecules embedded in quantum liquid clusters.^{11–13}

Van der Waals complexes undergo a variety of vibrations and rotations, including both intramolecular and intermolecular modes. For atom-diatom complexes $AB-X$, i.e., “dimer” species, the nature of the bound states is well understood. Several different angular momentum coupling schemes which provide good bases for perturbation expansions in the different regimes of interaction strength may be identified.¹⁴ More complicated systems such as atom-spherical top van der Waals complexes have also been addressed.¹⁵ Essentially both close coupling and basis set (or basis set-DVR¹⁶) calculations of the bound states of virtually any dimer system can now be performed with high accuracy. Some calculations on trimeric systems $n=2$ have also been made,^{17,18} but in general these methods are restricted to low dimensionality, and cannot be used for the investigation of larger complexes. This limitation of dimensionality for theoretical studies was until recently not regarded as unduly restrictive, since high resolution spectroscopy of heterogeneous van der Waals clusters was restricted to very small

clusters, with $n=1$ or 2.^{19–21} Therefore there was no compelling impetus to develop methods for the determination of energy levels for molecular chromophores in larger clusters. This situation has changed in recent years, with increasing numbers of spectroscopic experiments probing the energetics of larger clusters.^{22–26} One specific motivation for this work is provided by the recent high resolution spectra of molecules embedded in helium clusters,^{11,13} where the infrared absorption spectra of a number of small molecules in $^4\text{He}_n$ have been consistently found to display rotational structures compatible with an interpretation in terms of free rotor energy level patterns associated with rotational constants which are decreased relative to the gas phase values. Another motivation is provided by the observation of tunneling splittings in spectra of water clusters, over a range of sizes.^{26,27} Both of these classes of experiments demand an analysis in terms of energy levels for clusters containing molecular components, for nontrivial cluster size. Because of this perceived need to go to larger sizes, we have therefore pursued the Monte Carlo approach. As will be shown below, the combination of a MC calculation and maximum entropy analysis in the POITSE method offers a potentially powerful approach to deal with higher dimensional systems. The only size restriction at present is computer time, which can in principle be addressed by parallelization of the code to allow actual calculations for larger n values than those shown here.

The paper is organized as follows. In Sec. II we introduce the interaction potential for the $AB-X_n$ complex and describe the reference calculations performed by the DVR-FBR approach for the $AB-X$ dimer system. In Sec. III we review the POITSE method, introduce the trial wave function used in the Monte Carlo algorithm and discuss the choice of projection operators. POITSE results for $AB-X_n$, $n=1–3$, are presented in Sec. IIID. Section IV presents transition intensities for the dimer $AB-X$ and uses these to relate the energy levels calculated by POITSE for larger clusters to the empirical energy level patterns derived from spectroscopic experiments. Section V summarizes, and discusses possible extensions and future applications.

II. INTERACTION POTENTIAL AND $AB-X$ DIMER REFERENCE CALCULATIONS

A. Potential surface

The systems addressed here are heteronuclear van der Waals clusters of the form $AB-X_n$. We employ for these a model potential surface which is constructed to satisfy several criteria. First, we require that the main general features of van der Waals complexes are taken into account, in particular the energy scale and range of anisotropy. Second, we desire a fairly simple interpretation of the potential surface to avoid unnecessarily expensive computations. Third, since our specific interest lies in complexes of helium with molecules, we desire a model surface appropriate to one of the experimentally studied chromophores in helium clusters. To satisfy these requirements, we have constructed a simple, reduced dimensionality model for the much-studied interaction of He with SF_6 .^{28–30} This consists of a two-dimensional

model potential which retains the relative energetics of the full (rigid body) three-dimensional potential,²⁸ but which refers to a diatomic molecule with the mass and vibrational frequency of SF₆, rather than to the actual octahedral SF₆ molecule.

We will formulate the equations here using atomic units since the calculations are performed in these. In Secs. II C and III D, energies are given in cm⁻¹, the traditional units of vibration-rotation spectroscopy. Consider a diatomic molecule *AB* with attached atoms *X*₁...*X*_{*n*}. The masses of *A* and *B* are fixed, while the mass of the atoms *X*_{*i*}, *i*=1,...,*n*, will be varied. We use Jacobi-like coordinates *r*, *R*_{*i*} and *θ*_{*i*} and the distances *r*_{*ij*} between atoms *X*_{*i*} and *X*_{*j*} located at **r**_{*i*} and **r**_{*j*}, respectively,

$$\mathbf{r} = \mathbf{r}_A - \mathbf{r}_B, \quad (1)$$

$$\mathbf{r}_{\text{cm}} = \frac{m_A \mathbf{r}_A + m_B \mathbf{r}_B}{m_A + m_B}, \quad (2)$$

$$\mathbf{R}_i = \mathbf{r}_i - \mathbf{r}_{\text{cm}}, \quad (3)$$

$$\theta_i = \arccos \left[\frac{\mathbf{r}_i \cdot \mathbf{R}_i}{r R_i} \right]. \quad (4)$$

For *i*>1 a polar coordinate description would characterize each *X*_{*i*} atom by *R*_{*i*}, *θ*_{*i*} and an azimuthal angle *φ*_{*i*} relative to the plane spanned by *A*, *B*, and *X*₁. For convenience, in the formulation of the model potential we use interparticle distances *r*_{*ij*} instead of *φ*_{*i*}.

The total potential is written as a sum of a harmonic potential *V*_{HO}(*r*) for the intramolecular degree of freedom, an angle-modulated Morse oscillator potential *V*_{MO}(*R*_{*i*}, *θ*_{*i*}) for the van der Waals modes between *AB* and the atoms *X*_{*i*}, and a pair potential *V*_{XX}(*r*_{*ij*}) describing the *X*_{*i*}-*X*_{*j*} interaction,

$$V_{\text{total}} = V_{\text{HO}}(r) + \sum_{i=1}^n V_{\text{MO}}(R_i, \theta_i) + \sum_{i < j}^n V_{\text{XX}}(r_{ij}), \quad (5)$$

with

$$V_{\text{HO}}(r) = \frac{1}{2} \mu_r \omega_{\text{HO}}^2 (r - r_e)^2, \quad (6)$$

$$V_{\text{MO}}(R, \theta) = V_{\theta}(\theta) \cdot V_R(R), \quad (7)$$

$$V_R(R) = \exp[-2a(R - R_e)] - 2 \exp[-a(R - R_e)], \quad (8)$$

and

$$V_{\theta}(\theta) = D_e^{(0)} + D_e^{(4)} P_4(\cos \theta). \quad (9)$$

The potential for the diatomic part of the model system is harmonic, but evidently not the “simple harmonic oscillator,” which has a coordinate range from $-\infty$ to ∞ . The reduced mass of the diatomic molecule *AB* is $\mu_r = m_A m_B / (m_A + m_B)$. The parameters *r*_{*e*}, μ_r , *R*_{*e*}, *a*, *D*_{*e*}⁽⁰⁾, and *D*_{*e*}⁽⁴⁾ are chosen to model the SF₆-He interaction potential of Pack *et al.*²⁸ Since the potential contains no coupling of the intramolecular vibrational coordinate with the van der Waals coordinates, and thus cannot lead to any vibrational shift of *AB*, we choose ω_{HO} to match the actual ν_3 frequency

TABLE I. Potential parameters for the *AB*-*X* interaction, *V*_{HO}(*r*) + *V*_{MO}(*R*, *θ*), Eqs. (5)–(9), fit to emulate the principal features of the SF₆-He interaction as described in the text. The *AB* molecular parameters yield the gas phase rotational constant of SF₆, *B*₀=0.091 cm⁻¹.

<i>r</i> _{<i>e</i>} [<i>a</i> ₀]	ω_{HO} [cm ⁻¹]	μ_r [<i>m</i> _{<i>e</i>}]	<i>R</i> _{<i>e</i>} [<i>a</i> ₀]	<i>a</i> [<i>a</i> ₀ ⁻¹]	<i>D</i> _{<i>e</i>} ⁽⁰⁾ [cm ⁻¹]	<i>D</i> _{<i>e</i>} ⁽⁴⁾ [cm ⁻¹]
5.900	947.98	34631.970	7.951	0.92479	41.349	-22.463

of the free SF₆ molecule, $\nu_3 = 947.98 \text{ cm}^{-1}$.³¹ The rotational constant *B*_{*e*} of the free diatomic molecule *AB* is given by

$$B_e = \frac{1}{2 \mu_r r_e^2}. \quad (10)$$

Due to the symmetric nature of the diatomic potential and the stiffness of the oscillator, *B*_{*e*} approximates the ground state rotational constant *B*₀ to very high accuracy. Consequently, we choose *r*_{*e*} so that *B*_{*e*} ≈ *B*₀ is equal to the rotational constant of SF₆ in its ground vibrational state, *B*₀ = 0.091 cm⁻¹,³¹ requiring that the size of the diatomic be comparable to SF₆. This is achieved by selecting the masses *m*_{*A*} = *m*_{*B*} = 2 *m*_{*F*}.

The angle-modulated Morse potential is constructed to provide a reduced dimensionality model of the full anisotropic rigid SF₆-He potential *V*_{SF₆He}(*R*, *θ*, *φ*) of Pack *et al.*²⁸ This is a function of the two spherical polar angles *θ* and *φ* describing the orientation of a He atom in a molecule-fixed axis system. To arrive at a reduced dimensionality model, we integrate *V*_{SF₆He}(*R*, *θ*, *φ*) over the azimuthal angle, yielding

$$\tilde{V}_{\text{SF}_6\text{He}}(R, \theta) = \frac{1}{2\pi} \int_0^{2\pi} V_{\text{SF}_6\text{He}}(R, \theta, \phi) d\phi. \quad (11)$$

The *θ*-modulated Morse form of Eqs. (7)–(9) is then fit to a two-dimensional grid of values of $\tilde{V}_{\text{SF}_6\text{He}}(R, \theta)$, yielding the parameters *R*_{*e*}, *a*, *D*_{*e*}⁽⁰⁾, and *D*_{*e*}⁽⁴⁾.

Parameter values for *V*_{HO}(*r*) and *V*_{MO}(*R*, *θ*) are summarized in Table I. Figure 1 shows a comparison of the angle

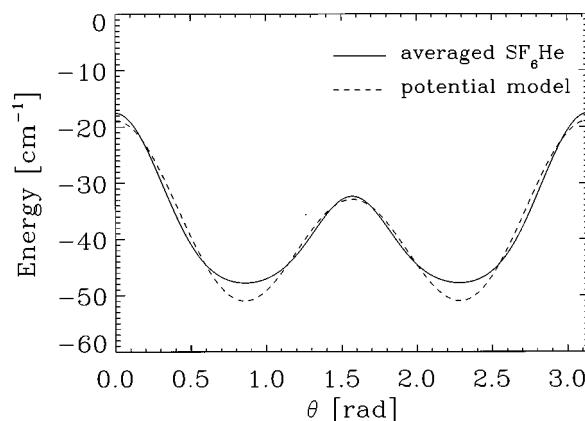


FIG. 1. Model potential for the system *AB*-*X*, constructed to emulate the features of the SF₆-He potential of Ref. 28 in a reduced dimensionality model. The dashed line shows a cut through the model potential, Eq. (5), as a function of *θ* for *r* = *r*_{*e*} and *R* = *R*_{*e*}. The solid line shows the integrated potential surface for SF₆-He, Eq. (11), with *R* = *R*_{*e*}.

dependence of the fitted model $V_{\text{MO}}(R, \theta)$ with that of the averaged potential $\tilde{V}_{\text{SF}_6\text{He}}(R, \theta)$ at the equilibrium value $R = R_e$. The $^4\text{He}-^4\text{He}$ potential of Aziz³² is used for the pair potential $V_{XX}(r_{ij})$. For calculations with $n=1$ we use a range of values for m_X , i.e., $m_X = (3/4)m_{\text{He}}, m_{\text{He}}, 2m_{\text{He}}, 3m_{\text{He}}, 4m_{\text{He}}$, and $5m_{\text{He}}$. For $n > 1$ we use $m_X = m_{\text{He}} = 4.0026$ amu only.

The angular modulation of the Morse potential in Eq. (7) results in an angle-dependent dissociation energy of the Morse oscillator in R , with a maximum value of 50.98 cm^{-1} at $\theta = 49^\circ$. The one-dimensional potential $V_{\text{MO}}(R, \theta = 49^\circ)$ supports two bound states, with energies -28.1 and -2.6 cm^{-1} , giving a one-dimensional stretching frequency of 25.5 cm^{-1} . This is somewhat larger than the first excitation of the van der Waals stretch which is obtained with the full potential (Sec. II C).

For $n=1$, the ground state energy derived from the model potential V_{total} can be estimated approximately as the sum of harmonic and one-dimensional Morse ground state energies, $E_{\text{HO},0} + E_{\text{MO},0}$. For $m_X = m_{\text{He}}$, $E_{\text{HO},0} = 474.0 \text{ cm}^{-1}$ while $E_{\text{MO},0}(\theta = 49^\circ) = -28.1 \text{ cm}^{-1}$. Thus the total energy of the system is positive and very large, relative to the low energy excitations connected with van der Waals coordinates. The latter are of primary interest in understanding the rotational excitations. The energy differences we are looking for are therefore about three orders of magnitude smaller than the total ground state energy, which is dominated by the zero point motion of the intramolecular vibration of AB .

B. DVR-FBR calculations for the $AB-X$ dimer: Theory

We describe here the Hamiltonian for the dimer, $AB-X$, and the combined discrete variable and finite basis representations used to solve for its eigenvalues. The Jacobi coordinates r, R , and θ were defined previously in Eqs. (1)–(4). Transforming to the center of mass coordinate frame and working in polar coordinates,

$$\begin{aligned}\cos \vartheta_r &= (z_A - z_B)/r, \\ \cos \varphi_r &= (x_A - x_B)/r_{xy}, \\ \cos \vartheta_R &= -(m_A z_A - m_B z_B)/(\mu_R R), \\ \cos \varphi_R &= -(m_A x_A - m_B x_B)/(\mu_R R_{xy}),\end{aligned}\quad (12)$$

with

$$\mu_R = \frac{m_X(m_A + m_B)}{m_X + m_A + m_B}, \quad (13)$$

and x_A, x_B, z_A , and z_B representing Cartesian components of \mathbf{r}_A and \mathbf{r}_B , leads to the following form of the rovibrational kinetic energy ($\hbar = 1$ as indicated earlier),

$$T = \sum_{q=r,R} \left[T_{\text{str}}(q) + \frac{1}{2\mu_q q^2} \hat{p}_q^2 \right], \quad (14)$$

$$T_{\text{str}}(q) = -\frac{1}{2\mu_q} \left(\frac{\partial^2}{\partial q^2} + \frac{2}{q} \frac{\partial}{\partial q} \right). \quad (15)$$

Here \hat{l}_q stands for the angular momentum operator defined by (ϑ_q, φ_q) and q_{xy} is the projection of the vector \mathbf{q} on the (xy) -plane ($\mathbf{q} = \mathbf{r}, \mathbf{R}$). The reduced masses corresponding to the stretching coordinates are μ_r (defined above) and μ_R [Eq. (13)]. The associated volume element $d\Omega$ is

$$d\Omega = r^2 dr R^2 dR \sin \vartheta_r d\vartheta_r d\varphi_r \sin \vartheta_R d\vartheta_R d\varphi_R. \quad (16)$$

Molecular rotation is made explicit by introducing an axis frame embedded by means of an orthogonal transformation parametrized by three Euler angles $(\varphi, \vartheta, \psi)$. For a triatomic complex the Euler angles are specified by: (i) defining the z -axis of the molecular frame to be along one of the two Jacobi vectors, and (ii) requiring that the vectors (\mathbf{r}, \mathbf{R}) span the (zx) molecular plane. The preferred choice of z -axis depends on the relative masses of the species, and should be made to approximate a principal moment of inertia axis of the complex. Thus when X is heavy relative to AB (e.g., $X = \text{Ar}, AB = \text{HF}$), \mathbf{R} is a good approximation for a principal axis and so the z -axis is usually defined to lie along \mathbf{R} in this case. This is the most prevalent embedded reference frame, and is commonly referred to as the body-fixed (BF) frame in both scattering and bound state calculations.¹⁴ In contrast, for light atoms X , the principal axes of the complex will more closely approximate the molecular axes. Therefore for $AB-X$ with $X = \text{He}$, we prefer to define the bond vector \mathbf{r} as the z -axis of the moving reference frame. We shall refer to this alternative choice of embedded frame as the molecule-fixed (MF) reference frame, to avoid confusion with the more common BF frame defined above. Such a molecule-fixed frame has been used for close coupling calculations of small molecules with He.³³ A quantitative comparison of the relative merits of these two embedded frames for DVR-FBR bound state calculations is made below.

In the MF frame, the Euler angles are defined by

$$\begin{aligned}\varphi &= \varphi_r, \\ \vartheta &= \vartheta_r, \\ \cos \psi &= \frac{\cos \vartheta_r \cos \theta - \cos \vartheta_R}{\sin \vartheta_r \sin \theta}, \\ \sin \psi &= \frac{\sin \vartheta_R \sin(\varphi_R - \varphi_r)}{\sin \theta},\end{aligned}\quad (17)$$

where θ denotes the angle between the Jacobi vectors,

$$\cos \theta = \cos \vartheta_r \cos \vartheta_R + \sin \vartheta_r \sin \vartheta_R \cos(\varphi_r - \varphi_R). \quad (18)$$

In this MF reference frame the kinetic energy contribution is given by

$$\begin{aligned}T(\theta, r, R, \varphi, \vartheta, \psi) &= T_{\text{str}}(r) + T_{\text{str}}(R) + f(R, r) l^2(\theta, \psi) \\ &\quad + \frac{1}{2\mu_r r^2} \left[(\hat{L}^2 - 2\hat{L}_z^2) + 2i\hat{L}_y \frac{\partial}{\partial \theta} + 2\hat{L}_x \hat{L}_z \cot \theta \right],\end{aligned}\quad (19)$$

where $\hat{\mathbf{L}} = (\hat{L}_x, \hat{L}_y, \hat{L}_z)$ is the total angular momentum, and $l \equiv l_R$. The kinetic energy T_{str} of the stretching vibrations is the same as in Eq. (15). The effective rotational constant $f(R, r)$ attributed to the bending vibration is given by

$$f(R, r) = \frac{1}{2} \left(\frac{1}{\mu_R R^2} + \frac{1}{\mu_r r^2} \right). \quad (20)$$

We note that permuting the subscripts r and R in Eqs. (17)–(20) leads to the kinetic energy in the alternative, conventional BF coordinate system having the z -axis along the Jacobi vector \mathbf{R} .³⁴

A complete rovibrational basis set is formulated by adding basis functions for the radial degrees of freedom r and R to an angular basis. For the strongly bound, intramolecular r coordinate we use eigenfunctions of the diatomic potential $V_{\text{HO}}(r)$, expanded in a distributed Gaussian primitive basis. The resulting eigenfunctions and diatomic energy levels are indistinguishable from those computed for the corresponding nontruncated simple harmonic oscillator on the interval $-\infty$ to ∞ , as expected when r_e is sufficiently large. The R coordinate describes the van der Waals intermolecular stretch, which is extremely weakly bound for AB -He systems, and hence the eigenfunctions are very diffuse in this coordinate. Therefore we use a discrete variable representation in R , which does not need to be evenly spaced and which can therefore very efficiently represent diffuse eigenfunctions. In the angular coordinate we use a standard basis of associated Legendre functions, described below. The DVR-FBR representation used here is thus distinct from representations used in DVR calculations for triatomic systems, where the angular coordinate is generally expanded in a DVR and the radial coordinate in a distributed Gaussian basis (DGB).³⁵

The angular basis can be specified either in the space-fixed (SF) reference frame or in the embedded reference frame, where for the latter we shall assume the molecule-fixed (MF) reference frame from now on. The DVR-FBR calculations are made in the MF frame, but it is useful to show here the form of the angular basis functions in both MF and SF frames, since both are utilized in making connection with the POITSE calculations later (Sec. III). In the SF frame there are two orbiting vectors, \mathbf{r} and \mathbf{R} , which couple to give a state with total angular momentum $\mathbf{J} = \mathbf{I}_r + \mathbf{I}_R$, where \mathbf{I}_r is the angular momentum of the diatom and \mathbf{I}_R is the end-over-end angular momentum of the complex. We shall use the conventional notation that $l_r \equiv j$ and $l_R \equiv l$ in the SF frame. The angular basis functions in the SF frame are therefore given by

$$S_{jl}^{JM} = |JMjl\rangle = \sum_{m_j, m_l} (jm_j l m_l | JM) |jm_j\rangle |lm_l\rangle, \quad (21)$$

where the expansion coefficients $(\dots| \dots)$ are the usual Clebsch-Gordan coefficients. m_j and m_l are the magnetic quantum numbers of the angular momenta $\mathbf{j} = \mathbf{I}_r$ and $\mathbf{l} = \mathbf{I}_R$, respectively, defined as projections onto the Z -axis of the SF frame. For the embedded reference frames we use the notation that $j \equiv l_r$, $l \equiv l_R$ for the BF frame, and that $j \equiv l_R$, $l \equiv l_r$ for the MF frame used here, i.e., j and l are interchanged in the MF frame. In the MF frame, the angular basis functions are direct products of normalized associated Legendre functions \bar{P}_j^K and symmetric top eigenfunctions $|JKM\rangle$,

$$\bar{P}_j^K |JKM\rangle = \sqrt{\frac{2J+1}{8\pi^2}} \bar{P}_j^K(\cos\theta) e^{iM\varphi} d_{MK}^J(\cos\vartheta) e^{iK\psi}. \quad (22)$$

M and K are the projections of the total angular momentum \mathbf{J} on the Z -axis of the SF frame, and on the z -axis of the MF frame, respectively. The SF and MF basis functions are related by the expressions

$$|JMjl\rangle = (-1)^j \sum_{K=-J}^J (JKj-K|l0) \bar{P}_j^K |JKM\rangle, \quad (23)$$

$$\bar{P}_j^K |JKM\rangle = (-1)^j \sum_l (JKj-K|l0) |JMjl\rangle. \quad (24)$$

(Note that for $J=0$, the sums reduce to a single term and MF, SF and BF basis functions are all identical.) Since the molecular Hamiltonian is invariant under spatial inversion, we can replace the spherical top functions in Eq. (22) by parity-adapted basis functions $F_{M|K|}^{Jp}$ defined by

$$F_{M|K|}^{Jp} = \frac{1}{\sqrt{2(1+\delta_{K0})}} (|J|K|M\rangle + (-1)^{J+|K|+p} |J-|K||M\rangle), \quad (25)$$

with $J \geq |K| \geq 0$. For $|K| > 0$, we have even ($p=0$) parity states and odd ($p=1$) parity states, while for $|K|=0$ only $p=0$ is allowed. The full, parity-adapted angular basis functions in the MF representation are then given by the product $F_{M|K|}^{Jp} \bar{P}_j^{|K|}$. The Hamiltonian matrix then decouples into blocks labeled by even ($p=0$) and odd parity ($p=1$). In the absence of an external field, both J and M are conserved. Strictly conserved quantum numbers for eigenstates of the AB -X system in the MF representation are then the following: total angular momentum J , its SF projection M , parity p , and the ordinal number $n^{J,p}$ which specifies the eigenenergy ordering. The magnetic quantum number M does not appear explicitly in the Hamiltonian matrix, i.e., all M -blocks are equivalent. In addition, if AB is homonuclear, i.e., A_2 , then there is additional exchange symmetry in the angular degree of freedom θ , which we denote by $\sigma = +/ -$. The quantum index of the harmonic oscillator, v , is also a good quantum number, since there is no potential coupling between r and the van der Waals coordinates R and θ in the present model, and the kinetic coupling via the $1/r^2$ factor in Eq. (19) has only an extremely weak effect. (The diatom rotational constants evaluated for various eigenfunctions in r differ in the fifth decimal place only.)

Once the eigenvectors $|\alpha\rangle$ are calculated, we can evaluate various quantities yielding information on the extent of angular decoupling in the different reference frames. Thus the quantities $\mathcal{P}_{jl}^{Jp} = |\langle JMjl|\alpha\rangle|^2$ (SF representation) and $\mathcal{P}_{|K|j}^{Jp} = |\langle F_{M|K|}^{Jp}|\alpha\rangle|^2$ (MF representation) provide a quantitative measure of just how “good” the nonconserved angular quantum numbers are, i.e., l and j in the SF representation, and K and j in the MF representation. The difference between the BF and MF embedded formulations can be seen in the quantity $\mathcal{P}_{|K|}^{Jp} = \sum_j \mathcal{P}_{|K|j}^{Jp}$, which is the contribution of a

TABLE II. DVR-FBR and POITSE results obtained with MF projectors for selected eigenvalues for $AB-X$ and $m_X = m_{\text{He}}$. Excitation energies ω_J calculated by DVR-FBR and POITSE are given in columns five and seven, respectively. All excitation energies are measured relative to the ground state energy $E_0 = 449.97 \text{ cm}^{-1}$. The first column contains the DVR-FBR basis function $F_{M|K|}^{J,p} \bar{P}_j^{[K]}$ [Eq. (25)], which corresponds to the POITSE projection operator given in the sixth column. σ and $n^{J,p}$ are DVR quantum numbers. $\mathcal{P}_{|K|j}^{J,p}$ is the square of the coefficient of the basis function listed in column one, in the exact eigenfunction (see text for more details).

$F_{M K }^{J,p} \bar{P}_j^{[K]}$	σ	DVR		$\omega_J [\text{cm}^{-1}]$	POITSE with MF projectors	
		$n^{J,p}$	$\mathcal{P}_{ K j}^{J,p}$		Projector	$\omega_J [\text{cm}^{-1}]$
$F_{00}^{00} \bar{P}_0^0$	+	0	0.75	0.0	1	0.0
$F_{00}^{00} \bar{P}_1^0$	−	1	0.76	0.091	$\cos \theta$	0.091
$F_{00}^{00} \bar{P}_2^0$	+	2	0.79	6.977	$(3 \cos^2 \theta - 1)$	7.056
$F_{00}^{11} \bar{P}_0^0$	−	0	0.73	0.153	$\cos \vartheta_r$	0.150
$F_{00}^{11} \bar{P}_1^0$	+	1	0.70	0.214	$\cos \vartheta_r \cos \theta$	(0.228)
$F_{00}^{11} \bar{P}_2^0$	−	4	0.78	7.181	$\cos \vartheta_r (3 \cos^2 \theta - 1)$	7.307
$F_{01}^{10} \bar{P}_1^1$	−	0	0.68	0.612	$\sin \vartheta_r \sin \theta \sin \psi$	0.620
$F_{01}^{11} \bar{P}_1^1$	+	2	0.61	0.620	$\sin \vartheta_r \sin \theta \cos \psi$	0.603
$F_{01}^{10} \bar{P}_2^1$	+	1	0.94	0.716	$\sin \vartheta_r \cos \theta \sin \theta \sin \psi$	0.715
$F_{01}^{11} \bar{P}_2^1$	−	3	0.92	0.689	$\sin \vartheta_r \cos \theta \sin \theta \cos \psi$	0.671
$F_{00}^{20} \bar{P}_0^0$	+	0	0.68	0.456	$(3 \cos^2 \vartheta_r - 1)$	0.483
$F_{00}^{20} \bar{P}_1^0$	−	1	0.62	0.473	$(3 \cos^2 \vartheta_r - 1) \cos \theta$	(0.542)
$F_{00}^{20} \bar{P}_2^0$	+	6	0.75	7.586	$(3 \cos^2 \vartheta_r - 1)(3 \cos^2 \theta - 1)$	7.717
$F_{01}^{20} \bar{P}_2^1$	+	2	0.81	0.921	$\sin \vartheta_r \cos \vartheta_r \cos \theta \sin \theta \cos \psi$	0.937
$F_{01}^{21} \bar{P}_1^1$	−	0	0.65	0.921	$\sin \vartheta_r \cos \vartheta_r \cos \theta \sin \theta \sin \psi$	1.050
$F_{01}^{20} \bar{P}_1^1$	−	3	0.48	0.929	$\sin \vartheta_r \cos \vartheta_r \sin \theta \cos \psi$	(0.809)
$F_{01}^{21} \bar{P}_2^1$	+	1	0.88	0.994	$\sin \vartheta_r \cos \vartheta_r \sin \theta \sin \psi$	0.976
$F_{02}^{20} \bar{P}_2^2$	+	4	0.56	2.182	$\sin^2 \vartheta_r \sin^2 \theta \cos(2\psi)$	2.169
$F_{02}^{21} \bar{P}_2^2$	−	2	0.56	2.187	$\sin^2 \vartheta_r \sin^2 \theta \sin(2\psi)$	(2.140)

particular $|K|$ subspace to a given eigenfunction. The larger this quantity, the greater the extent of decoupling in that representation.

The Hamiltonian matrix was set up with 120 points in the DVR basis for R , obtained by diagonalizing the operator \hat{R} in a primitive basis of unevenly distributed Gaussians. The resulting DVR points R_z cover the range $6a_0 < R < 240a_0$, but the first 35 points spanning $6a_0 < R < 50a_0$ are sufficient to represent all states of interest. At each DVR point R_z , we first solve the two-dimensional problem in r and θ , retaining only one diatomic eigenfunction for the r -coordinate and using a basis of Legendre functions for θ . Both kinetic and potential matrix elements in θ can then be evaluated analytically. The resulting two-dimensional representation is truncated at 51×51 for all R_z . These eigenvectors are then combined with the DVR points and the parity-adapted basis functions to assemble a block matrix labeled by (J, p, K) , to which are added the kinetic couplings between DVR points and the diagonal matrix elements deriving from overall rotation in Eq. (19). These blocks are prediagonalized, and then the remaining off-diagonal $(K, K \pm 1)$ coupling is added. The final diagonalization yields eigenvectors labeled only by $(J, p, n^{J,p})$. At convergence, both the prediagonalization and the final diagonalization involve matrices of order 1000×1000 .

C. DVR-FBR calculations for the $AB-X$ dimer: Results

The DVR-FBR calculations were all carried out for the mass combination $m_A = m_B = 2m_F$ and $m_X = m_{\text{He}}$. Bound-state DVR-FBR results for selected (low-energy) eigenstates are presented in the left hand section of Table II. All eigenenergies are shown as excitation energies ω_J (column five) relative to the van der Waals ground state reference $E_0 = -24.019 \text{ cm}^{-1}$, which is measured relative to the lowest dissociation channel of the system. This channel corresponds to the diatomic in its ground vibrational state and is located 473.99 cm^{-1} above the potential minimum. The actual calculations explicitly include this oscillator (see also the discussion in Sec. II A). The strictly conserved quantum numbers J and p can be extracted from the superscripts of the angular basis function listed in the first column, while σ and $n^{J,p}$ are given explicitly in columns two and three, respectively. Column four shows the probability $\mathcal{P}_{|K|j}^{J,p}$ of the dominant contributing decoupled state $F_{M|K|}^{J,p} \bar{P}_j^{[K]}$ (column one) to the eigenstate associated with ω_J . This gives an approximate state assignment.

The exchange symmetry quantum number σ is calculated by evaluating the overlap integral

$$\sigma = \text{sign} \left[\int \psi_\alpha^*(\mathbf{r}, \mathbf{R}) \psi_\alpha(-\mathbf{r}, \mathbf{R}) d\Omega \right] \quad (26)$$

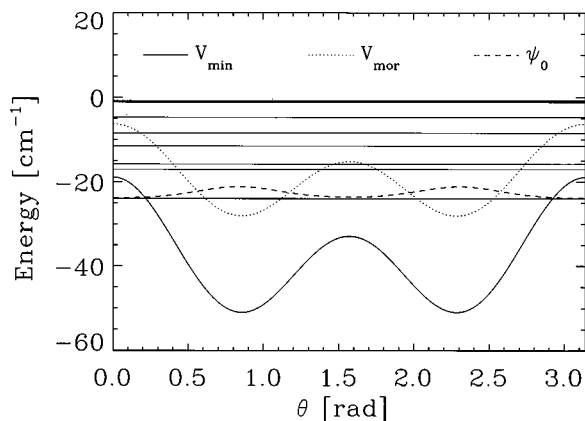


FIG. 2. Bound state energy levels for $J=0$, minimum energy paths, and ground state wave function ψ_0 of the model system $AB-X$. V_{\min} (solid line) is the minimum energy path along the Jacobi angle θ , obtained by optimizing the Jacobi coordinates r and R at each angle. V_{mor} (dotted line) is the adiabatic path along θ including the zero-point energy contribution of the Morse oscillator along R . ψ_0 (dashed line) is a cut through the ground state wave function with r and R fixed at their ground state expectation values. The complete set of ten bound states (-24.019 , -23.928 , -17.042 , -15.785 , -11.496 , -8.403 , -4.706 , -1.141 , -0.907 , and -0.796 cm^{-1}) is shown as horizontal solid lines. The small tunneling splitting between the first two states and the dense group of three states just below the dissociation limit cannot be resolved on the energy scale of the graph.

for each eigenfunction $\alpha \equiv \psi_\alpha$, where $d\Omega$ is the volume element of Eq. (16). This results in exchange symmetry $\sigma = +$ and $-$ for eigenstates that are, respectively, symmetric and antisymmetric under permutation of the identical atoms A and B .

The full model potential of Eq. (5) supports ten bound states for the rotationless complex ($J=0$), and nine bound states for $J=1$ with even parity ($p=0$). No positive energy bound states for $J=1$, $p=0$ are found below the $j=1$ AB state, which lies at $+0.182$ cm^{-1} . All bound states are fully delocalized in θ .

Figure 2 shows the $J=0$ energy levels together with the bare minimum energy path $V_{\min}(\theta)$ (lower curve) and with the minimum energy path $V_{\text{mor}}(\theta)$. The latter differs from $V_{\min}(\theta)$ by the additional zero-point energy of the Morse oscillator in R , and can therefore be regarded as the first potential adiabat. The eight angularly excited bound states shown here clearly develop a free-rotor-like pattern at energies above -15 cm^{-1} , suggesting that for $J=0$ the AB diatom is behaving like a hindered rotor, with vibrational bending motion in the lowest levels being supplanted by free rotation at energies above the angular barriers.

As outlined in Sec. II B, the probability $\mathcal{P}_{|kl|j}^{jp}$ quantifies the quality of the state assignments in column one of Table II. For $J=0$ and $l=j=0$, MF and SF basis functions are equivalent, so the value of \mathcal{P}_{00}^{00} can be used to assess the extent of angular coupling in an SF frame. In the fully decoupled limit, i.e. no angular potential, \mathcal{P}_{00}^{00} is unity in the ground state. We find instead that $\mathcal{P}_{00}^{00}=0.75$. This reduction in \mathcal{P}_{00}^{00} indicates the presence of an appreciable amount of potential coupling between the rotor eigenfunctions in the SF frame. Consequently, the first four levels in Fig. 2 may indeed be considered as pure vibrational states.

In contrast, the energy spacing between the higher levels

with $n^{0,0}=4,5$, and 6 is readily interpreted in terms of free internal rotation. These level spacings Δ_j can be remarkably well described by

$$\Delta_j = E_{j+1} - E_j = 2f(j+1). \quad (27)$$

The value for f of 0.309 cm^{-1} computed from $j=4, 5$, and 6 agrees perfectly with the value of the rotational constant for the bending vibration predicted by Eq. (20) using Eq. (10) and the values in Table I. The ground state expectation value of R , $\langle R \rangle = 8.50a_0$, gives an estimate of 0.218 cm^{-1} for the end-over-end ground state rotational constant B_0^R . The value of $\langle R \rangle$ is only weakly dependent on the angular excitation, varying from the ground state value $\langle R \rangle = 8.50a_0$ for $n^{0,0}=0$, to $8.79a_0$ for $n^{0,0}=6$. This is not surprising given that the minimum value of R is angle-independent in this model [Eq. (7)]. Examination of the eigenfunctions shows that this energetically derived picture of free internal rotation is more complicated, however. The probabilities \mathcal{P}_{0j}^{00} are now much lower, ~ 0.6 for $n^{0,0}=4,5,6$, which indicates the importance of the angular coupling also above the adiabatic barrier. A similar distinction between energetics which show nearly free internal rotation and eigenstates which show strong mixing has been observed in calculations of rovibrational excitations of $\text{NH}_3\text{-Ar}$.³⁶

The full potential supports a single $\sigma = +$ van der Waals stretch excited state ($n^{0,0}=7$). This is weakly bound at -1.14 cm^{-1} , resulting in a van der Waals stretching frequency of 22.88 cm^{-1} . This is somewhat lower than the maximum one-dimensional frequency obtained for $V_{\text{MO}}(R, \theta)$ (Sect II A). In the excited stretch state we find $\mathcal{P}_{00}^{00}=0.94$. Such a high value implies near perfect decoupling and therefore suggests that excitation of the van der Waals stretch leads now to an almost perfectly free rotation of the diatom AB .

The rotational behavior of the $AB-X$ dimer was studied for $J \leq 6$, in both parities. For $J=1$ we compared the two possible embeddings of the z -axis of the moving reference frame. The superiority of the MF representation relative to the BF representation can be seen from inspection of the probability $\mathcal{P}_{|kl|j}^{jp}$ defined above. In the ground vibrational state and with $K=0$, this is equal to 0.98 in the MF representation, but is only 0.55 in the BF. Therefore we conclude that the MF representation provides a greater decoupling and K is a better quantum number in this embedded representation.

Effective rotational constants A , B , and C can be calculated for the ground vibrational state from the $J=0$ and $J=1$ energies, using the standard equations for the three $J=1$ sublevels of an asymmetric top.³⁷ These yield $A=0.539$, $B=0.081$, and $C=0.073$ cm^{-1} , and hence a value of $\kappa = -0.97$ for Ray's asymmetry parameter.³⁸ Therefore the dimer behaves as a nearly prolate symmetric top. Values for the effective symmetric top constants, $\bar{B} = (B+C)/2$, and the centrifugal distortion constant D in the ground vibrational state were obtained by fitting the rotational levels for $J=0-6$, $K=0$ to the symmetric top $K=0$ expression,

$$E_J = \bar{B}J(J+1) - DJ^2(J+1)^2. \quad (28)$$

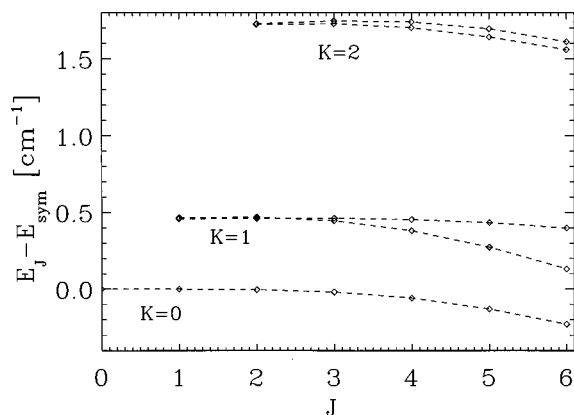


FIG. 3. Asymmetry splitting of rotational levels of the $AB-X$ model system with $m_X = m_{He}$. Rotational energies for several K -sublevels are plotted vs J , relative to the symmetric top contribution $E_{sym} = \bar{B}J(J+1)$ [Eq. (28)]. Asymmetry splitting becomes relevant at $J \geq 4$. See also discussion in Sec. IV and the computed band contours in Fig. 7.

This yields $\bar{B} = 0.077$ and $D \approx 2 \cdot 10^{-4} \text{ cm}^{-1}$. Asymmetry becomes more important at larger K values, as is evident from Fig. 3, which shows the deviation from the symmetric top energies, $E_j - \bar{B}J(J+1)$ as a function of J , for several K values, in the ground vibrational state. (The centrifugal distortion term has a negligible effect on this energy scale.) We see that the symmetric top is a very good description up to $J=3$ for all K values shown here, but that for $J>3$ the energy levels show significant deviations from this model.

III. POITSE CALCULATIONS

A. Methodology

The POITSE method allows the calculation of excited state energies from a stochastic solution of the Schrödinger equation. The approach is based on a combination of zero temperature quantum Monte Carlo and maximum entropy image reconstruction methods, and has the advantage of not imposing any nodal approximations. The basic formulation has been discussed in detail in previous papers.⁵⁻⁷ Therefore we will restrict ourselves here to a short summary of the main ideas, and of features specific to the $AB-X_n$ systems treated here.

POITSE is based on the calculation of an imaginary time correlation function, whose Laplace inverse yields the spectrum of excitations (hence the name “imaginary time spectral evolution”). A key feature of the method is the presence of a projection operator, \hat{A} , which allows the sequential extraction of excited states and which significantly facilitates the numerical Laplace inversion. The starting point is the spectral weight function, $\kappa(\omega)$,

$$\kappa(\omega) = \sum_f |\langle \psi_i | \hat{A} | \psi_f \rangle|^2 \delta(E_i - E_f + \omega), \quad (29)$$

where ψ_i and ψ_f are initial and final eigenstates of the system having energies E_i and E_f , respectively. Performing a two-sided Laplace transform results, after some simplifications, in

$$\tilde{\kappa}(t) = \int_{-\infty}^{\infty} \exp(-\omega t) \kappa(\omega) d\omega \quad (30)$$

$$= \langle \psi_i | \hat{A} \exp[-(H - E_i)t] \hat{A}^+ | \psi_i \rangle, \quad (31)$$

where t is now identified with the imaginary time of a DMC propagation and H is the Hamiltonian of the system. These matrix elements, which now involve only the initial state, can be evaluated by making a multidimensional MC integration over the distribution $|\psi_i|^2$ and performing a DMC side-walk at each MC point. As discussed in Ref. 5, the exact initial state ψ_i is approximated by a trial wave function ψ_T and the initial energy E_i by the reference energy E_{ref} .

The DMC propagation must be guided by a nodeless, positive guiding wave function ψ_G .^{2,39} In general, this guiding function can differ from the trial wave function ψ_T which is used for the calculation of expectation values and which may have some nodal structure. Guiding functions are generally used to increase the efficiency of a simulation by directing the sampling to the important regions of configuration space. In this work we use the simplest version of the POITSE algorithm, in which the guiding and trial functions are identical and both approximate the exact ground state wave function. This yields energy differences from the ground state reference. More generally, one can construct a POITSE algorithm for energy differences from an arbitrary known excited state, using a positive guiding function which could be, for example, an approximation to the exact ground state, together with a trial function ψ_T which approximates the excited state reference.⁴⁰ Sampled expectation values are then those of the excited state reference, which contains some nodal structure, and the energy differences extracted from Eq. (29) are referred to this state.

Normalization of Eq. (31) eliminates the dependence of the spectrum on the arbitrary reference energy E_{ref} and results in a spectrum where the excited state energies are expressed relative to the exact ground state energy of the system,

$$\tilde{\kappa}(t) = \frac{\langle \psi_T | \hat{A} \exp[-(H - E_{ref})t] \hat{A}^+ | \psi_T \rangle}{\langle \psi_T | \psi_T \rangle} \cdot \frac{\langle \psi_T | \exp[-(H - E_{ref})t] | \psi_T \rangle}{\langle \psi_T | \psi_T \rangle}. \quad (32)$$

The MC evaluation of this equation is given by

$$\tilde{\kappa}(t) = \frac{\frac{1}{P} \sum_{k=1}^P \hat{A}^+(R_k^{(0)}) \hat{A}(R_k^{(t)}) w(R_k^{(t)}, \Delta t)}{\frac{1}{P} \sum_{k=1}^P w(R_k^{(t)}, \Delta t)}, \quad (33)$$

where the initial configurations $R_k^{(0)}$ are sampled from $|\psi_T(R)|^2$ using a standard MC walk and $w(R_k^{(t)}, \Delta t)$ are the weights of the random walkers in the DMC sidewalk originated at $R_k^{(0)}$.

The MC implementation is illustrated here for the example of the $AB-X$ dimer. In the present calculations we move all atoms independently so that all samplings are nine dimensional. This implicitly includes the center of mass and

overall rotational motions. The corresponding DVR calculation for the $AB-X$ system explicitly treats only the three internal degrees and the three overall rotational degrees of freedom, and so is only six dimensional. While removal of the center of mass motion from the POITSE calculation would reduce the dimensionality, it does, however, introduce complications for the treatment of rotational motions.⁴¹ Such complications are avoided when all particles are moved independently. (Completely independent Cartesian moves of all atoms are possible only as long as the potential surface is a function of all internal coordinates. Thus a flexible vibrator, as in the current model for AB , is in fact technically easier to deal with than a rigid rotor diatomic, for which independent cartesian moves of all atoms have to be combined with adiabatic constraints to ensure rigidity.⁴²) Thus in the present calculations, a configuration is defined by the coordinates (x_i, y_i, z_i) of all atoms. The outer MC walk creating the initial configurations $R_k^{(0)}$ in the nine-dimensional configuration space is performed with the Metropolis algorithm, i.e., all three coordinates x_i, y_i , and z_i of each atom are sampled according to the square of the trial wave function $|\psi_T|^2$. However, the potential function and the sampling function are both parametrized as functions of body-fixed coordinates, as described in Secs. II A and III B. The trial function is constructed to have zero center of mass translation energy and zero overall angular momentum, so that while translation and rotational motions are implicitly incorporated, the true cluster ground state energy would nevertheless be obtained from a pure DMC walk.

For the DMC sidewalks we employ the algorithm often referred to as the “pure” DMC algorithm, in which branching processes are not incorporated.^{2,39} In DMC, configurations advance in imaginary time t according to three elementary processes, diffusion, drift, and population growth, to create an evolving series of configurations $R_k^{(t)}$. Population growth is often simulated by branching, i.e., creating replicas of configurations. This branching process is not an essential component per se, however, since population growth may alternatively be taken into account by introducing variable weights for each configuration. In that case the number of walkers remains constant. In a DMC ground state calculation this can cause stability problems since the cumulative weight $w(R_k^{(t)}, \Delta t)$,

$$w(R_k^{(t)}, \Delta t) = \prod_{j=1}^{j_{\max}} \exp \left\{ - \left[\frac{1}{2} (E_L(R_k^{(j\Delta t)}) + E_L(R_k^{((j-1)\Delta t)})) - E_{\text{ref}} \right] \Delta t \right\}, \quad (34)$$

$$t = j_{\max} \Delta t,$$

of a walker may become very large or very small, which necessitates that walkers be split or annihilated in a somewhat artificial fashion. In the sidewalks, however, we are interested in the evolution of this cumulative weight as a continuous function of the imaginary time, and not only at asymptotic times as is the case when one is interested in projecting out the ground state wave function. In order to avoid any possible complications or inconsistencies between

the inner DMC sidewalk and the outer MC sampling which might arise from appearing or disappearing DMC walkers, we do not, therefore, make any such manipulation of the number of DMC walkers but rather use only the pure weights.

The cumulative DMC weight $w(R_k^{(t)}, \Delta t)$ depends on the initial configuration $R_k^{(0)}$, on the imaginary time propagated configurations $R_k^{(t)}$, and on the finite DMC step Δt . However, this cumulative weight does not depend on the projection operator \hat{A} . Therefore, Eq. (33) can be evaluated for several projection operators simultaneously. The additional computational effort for using more than one projection operator at a time is negligibly small, and so usually we run about eight different projection operators within one MC sampling.

The excited energies E_f of Eq. (29) are extracted by performing a two-sided numerical inverse Laplace transform of Eq. (33), using the Bayesian approach of the maximum entropy method⁴ within the formulation of Bryan.⁴³ This provides a stable inversion procedure as long as the spectra consist of isolated features, as discussed in Ref. 7. In the maximum entropy method, the inverse transform of Eq. (33) is constructed by maximizing the constrained entropy $Q = \alpha S - L$, where L is a least-square measure of the numerical error in $\tilde{\kappa}(t)$, α is a Lagrange parameter, and S is the Shannon-Jaynes entropy. S depends on a model for $\kappa(\omega)$, usually denoted as the default model $m(\omega)$. We use here the flat default model, i.e., $m(\omega) = \text{const}$. In Bryan's approach, problems associated with oversampling are avoided by expressing the optimal solution $\kappa(\omega)$ as the average over solutions $\kappa_{\text{opt}, \alpha}(\omega)$ which maximize Q for a given value of the parameter α .⁴

B. Trial wave function for $AB-X_n$

The form of the model potential surface, Eq. (5), suggests a product ansatz for our trial wave function ψ_T . This is written as a product of an r -dependent harmonic oscillator function $\phi_{\text{HO}}(r)$, an R -dependent Morse oscillator function $\phi_{\text{MO}}(R)$, which is further modulated by a θ -dependent function $\phi_{\theta}(\theta_i)$, and a product of Jastrow-like functions $\phi_{XX}(r_{ij})$,

$$\psi_T = \phi_{\text{HO}}(r) \cdot \left[\prod_{i=1}^n \phi_{\theta}(\theta_i) \cdot \phi_{\text{MO}}(R_i) \right] \cdot \left[\prod_{i < j} \phi_{XX}(r_{ij}) \right], \quad (35)$$

where

$$\phi_{\text{HO}}(r) = \frac{1}{r} \exp \left[- \frac{1}{2} \mu_r \omega_{\text{HO}} (r - r_e)^2 \right], \quad (36)$$

$$\phi_{\text{MO}}(R) = z^{((\omega_e/x_e) - 1)/2} \exp \left(- \frac{z}{2} \right),$$

$$z = \frac{\omega_e}{x_e} \exp[-a(R - R_e)], \quad (37)$$

and

$$\phi_{XX}(r) = \exp \left[- \ln 2 \left(\frac{P_{\text{He}}}{r} \right)^5 \right]. \quad (38)$$

TABLE III. Trial wave function parameters and reference energy used in POITSE calculations for $AB-X_n$ [Eqs. (35)–(39)].

m_X	n	p_1	p_2	$p_{\text{He}} [a_0]$	$E_{\text{ref}} [\text{cm}^{-1}]$
$(3/4)m_{\text{He}}$	1	2.0	1.0	...	452.12
m_{He}	1	2.0	1.0	...	452.12
$2m_{\text{He}}$	1	2.6	1.0	...	443.21
$3m_{\text{He}}$	1	2.8	1.0	...	440.26
$4m_{\text{He}}$	1	3.0	1.0	...	434.56
$5m_{\text{He}}$	1	3.2	1.0	...	432.36
m_{He}	2	2.0	0.8	5.5	425.93
m_{He}	3	2.0	0.8	5.5	401.64

The form of the angle-dependent part of the wave function $\phi_\theta(\theta)$ is determined by the modulations of the potential surface along the θ coordinate. The potential surface has its absolute maxima at $\theta=0$ and π and an additional smaller maximum at $\theta=\pi/2$ (Fig. 1). We therefore use the parametrization,

$$\phi_\theta(\theta) = \exp[p_1 \sin^2(2\theta) + p_2 \sin^2(\theta)], \quad (39)$$

which allows independent variation of $\phi_\theta(\theta)$ near the minima at $\theta=0$ and π , from that near the minimum at $\theta=\pi/2$. The parameters p_1 , p_2 , and p_{He} in ψ_T are obtained by standard variational optimization of the ground state energy. The parameter ω_e/x_e in Eq. (37) is fixed at the Morse value, such that $\phi_{\text{MO}}(R)$ solves the one-dimensional Schrödinger equation for a particle of mass μ_R in the potential $D_e^{(0)}V_R(R)$,

$$\frac{\omega_e}{x_e} = \frac{2}{a} \sqrt{2D_e^{(0)}\mu_R}. \quad (40)$$

We tried to improve the trial wave function ψ_T further by treating ω_{HO} [Eq. (36)] and R_e [Eq. (37)] as variational parameters. However, variational optimization of these two parameters did not result in any significant improvement of the ground state energy for the $AB\text{-}^4\text{He}$ system. Therefore, in the calculations reported below, these values are fixed at the values suggested by the model potential surface and listed in Table I. Table III summarizes the optimized parameters p_1 , p_2 , and p_{He} used in the POITSE calculations for all cluster sizes and values of m_X used here. For these small sizes, the helium-helium correlation parameter, p_{He} , is relatively insensitive to details of the $AB\text{-He}$ potential, and essentially the same value is used here as in DMC studies of HF-He_n which made use of the same Jastrow function.⁴⁴

The optimized product trial function ψ_T overestimates the exact ground state energy (Sec. II C) by less than 0.5%. Since the total energy is dominated by the vibrational energy of the harmonic oscillator, while we are here mainly interested in the much lower energy van der Waals excitations to which the ground state energy is not sensitive, the quality of ψ_T should ideally be monitored by additional criteria. Therefore we constructed an alternative trial function by making a numerical fit to the exact, DVR-FBR ground state wave function for the $AB\text{-}^4\text{He}$ dimer. The fit employs similar functional form to Eq. (35) but is more flexible, treating the parameter ω_e/x_e in ϕ_{MO} as a variational parameter, and expanding ϕ_θ as a fifth order polynomial in $\cos(\theta)$. For the

$AB\text{-}X$ system with $m_X = m_{\text{He}}$, we performed POITSE calculations using the SF projection operators (see below) for both ψ_T and this improved trial wave function. POITSE results from the two trial wave functions agree to within 2%, confirming that use of the trial function ψ_T given by Eqs. (35)–(40) does not bias the excitation energies.

C. Projection operators

In this section we describe the projection operators \hat{A} used in the POITSE calculations. To motivate this, we first review the projectors employed previously for two models of excitations, namely the vibrational and rotational excited states of a rotating oscillator.^{5–7} The vibrational excited states of a one-dimensional harmonic oscillator can be written as $(a^+)^n|\psi_0\rangle$, $n=1,2,\dots$, with $\psi_0(x)$ being the ground state wave function of the system. Since the creation operators $(a^+)^n$ can be expressed as polynomials in the oscillator coordinate x , x^n is therefore an appropriate choice for the projection operator accessing vibrational excitations for an oscillator.⁵ The calculation of rotational excitations for a rotating oscillator was based on the observation that the rotationally excited state wave functions can be expressed as $Y_{lm}(\theta, \phi)\psi_0(r)$, where the entire angle dependence is carried by the spherical harmonics. The projection operators can therefore be chosen as the spherical harmonics, $Y_{lm}(\theta, \phi)$, in this case.^{6,7}

The results of these prior calculations can be summarized by the following statement. A good projection operator \hat{A} is an operator which acts on the ground state wave function to produce an approximation to an excited state. Formally, it thus resembles the excitation operators often used in many-body problems.⁴⁵ Because of the maximum entropy inversion contained in the current POITSE algorithm, the greater the overlap with a single excited state, the better the resolution afforded by POITSE. This is easily seen by consideration of the extreme case in which \hat{A} acts on the ground state to produce an exact excited state wave function. In this case the POITSE signal $\tilde{\kappa}(t)$ consists of a single exponential decay, and the corresponding $\kappa(\omega)$ spectrum is simply a single δ -peak. The inverse Laplace transform, which is in general an ill-posed problem for noisy input data, is in this case relatively easy to perform and guarantees a clear spectrum. However, if the product of the projection operator and the trial wave function is a superposition of two or more excited states, the inverse Laplace transform does not necessarily result in a $\kappa(\omega)$ spectrum consisting of well separated δ -peaks, but may give, e.g., broadened and/or asymmetric peaks. We shall refer to projection operators for which the POITSE algorithm results in a $\kappa(\omega)$ spectrum with well separated δ -peaks, as good projection operators.

We find such sets of good projection operators for the $AB\text{-}X_n$ system by analysis of the DVR-FBR calculations performed for the dimer system $AB\text{-}X$. For the dimer system, the simplest projection operators are those yielding the vibrationally excited states of the radial coordinates r and R . In analogy to the simple one-dimensional harmonic oscillator, we use $(r-r_e)^n$ and $(R-R_e)^n$ as projection operators for these excitations, noting that anharmonicity will modify

the optimal value of the index n . The intramolecular vibrational excitations are of higher frequency than the van der Waals excitations, and POITSE calculations for these modes are therefore performed using a smaller DMC time step than those for the van der Waals modes.

Projection operators accessing excitations associated with angular momentum are less straightforward. In DVR-FBR calculations, the angle dependent part of the wave function for a complex can be equivalently expanded in either a SF or MF representation (Sec. II B). Since POITSE gives the exact excitation energy as long as there is some reasonably big non-zero projection onto the excited state, the choice of representation used for the projectors should, in principle, also be irrelevant. In practice, however, because of the nonuniqueness associated with the spectral reconstruction mentioned above, it is desirable to use projectors which provide the greatest overlap with the excited state of interest. The choice of representation for clusters $AB-X_n$ will then be determined by this criterion, as well as by the ease of constructing the generalized projectors for $n > 1$.

The MF projection operators employed here to access excitations associated with angular coordinates are given by the unnormalized modulus of the full parity-adapted angular basis functions $F_{M|K}^{Jp} \bar{P}_j^{|K|}$ (these are either pure real or pure imaginary). Due to the M -degeneracy (Sec. II B), we can restrict ourselves to basis functions with $M=0$. For the other quantum numbers we have the following restrictions: $j \geq 0$; $K=0, \pm 1, \dots, \pm j$; $J \geq |K|$. The first column in the right hand section of Table II contains the MF operators for projectors derived from the dominant DVR-FBR basis function for each of the excited states listed in the left hand section.

Several additional calculations were carried out with an alternative set of molecule-fixed projectors defined as functions of the bond angle $\cos \chi = \mathbf{r}_{BX} \cdot \mathbf{r} / (r_{BX} r)$. These projectors mix the van der Waals bending and stretching degrees of freedom much more than MF projectors formulated through the Jacobi angle θ . Nevertheless they access essentially the same van der Waals bending states and similar excitation energies are obtained. However, the increased mixing leads to somewhat less well resolved peaks.

The SF projectors are derived from the SF angular basis functions, Eq. (21), where

$$|jm_j\rangle = Y_{jm_j}(\vartheta_r, \varphi_r),$$

$$|lm_l\rangle = Y_{lm_l}(\vartheta_R, \varphi_R). \quad (41)$$

The reader should bear in mind that in the SF frame, j refers to the diatom angular momentum l_r , and l to the end-over-end angular momentum l_R of the complex, i.e., the opposite of the notation in the MF frame (Sec. II B). SF projectors result from making real linear combinations of these basis functions for a given J, j and l . Examples of such projectors for $l=0$ are given in the first column of Table IV, and the explicit forms are given in the second column. We use the M -degeneracy to obtain an additional measure of the statistical spread in the POITSE results here, making calculations with several M values and averaging over the results. Thus for $j=1$ and $J=1$, we employ three projectors, corresponding to $M=0, \pm 1$; for $j=2$ and $J=2$, we have five projec-

TABLE IV. POITSE results for $AB-X$ with $m_X = m_{\text{He}}$ obtained using SF projection operators. The first and second column contain the POITSE projection operator used: $x = (x_A - x_B)$, $y = (y_A - y_B)$, and $z = (z_A - z_B)$. The mean peak position derived from each spectrum, $\omega_J = E_J - E_0$, is given in the third column. The quantity $\omega_{J,\text{ave}}$ in the fourth column lists the average of these mean peak positions over all substates of a specific J . The number in parentheses gives the standard deviation over these substate values. The fifth column gives the exact excitation energies obtained from DVR-FBR.

S_{jl}^{JM}	POITSE with SF projectors Projector	ω_J [cm ⁻¹]	$\omega_{J,\text{ave}}$ [cm ⁻¹]	DVR ω_J [cm ⁻¹]
S_{10}^{10}	z/r	0.158		0.153
$S_{10}^{11} + S_{10}^{1-1}$	y/r	0.155	0.158(3)	
$S_{10}^{11} - S_{10}^{1-1}$	x/r	0.160		
S_{20}^{20}	$(3z^2 - r^2)/r^2$	0.490		0.475
$S_{20}^{21} + S_{20}^{2-1}$	yz/r	0.481		
$S_{20}^{21} - S_{20}^{2-1}$	xz/r	0.479	0.479(3)	
$S_{20}^{22} + S_{20}^{2-2}$	xy/r	0.482		
$S_{20}^{22} - S_{20}^{2-2}$	$(x^2 - y^2)/r^2$	0.478		
S_{30}^{30}	$(5z^3 - 3r^2z)/r^3$	—		0.900
$S_{30}^{31} + S_{30}^{3-1}$	$y(5z^2 - r^2)/r^3$	0.942		
$S_{30}^{31} - S_{30}^{3-1}$	$x(5z^2 - r^2)/r^3$	—		
$S_{30}^{32} + S_{30}^{3-2}$	xyz/r^3	0.969	0.963(15)	
$S_{30}^{32} - S_{30}^{3-2}$	$z(x^2 - y^2)/r^3$	0.974		
$S_{30}^{33} + S_{30}^{3-3}$	$y(y^2 - 3x^2)/r^3$	0.978		
$S_{30}^{33} - S_{30}^{3-3}$	$x(x^2 - 3y^2)/r^3$	0.954		

tors, corresponding to $M=0, \pm 1, \pm 2$; for $j=3$ and $J=3$, seven projectors, etc. These SF projectors are isomorphic to the real representations of the angular functions for the hydrogen atom, e.g., ($j=1, J=1$) projectors are isomorphic to p -orbitals, ($j=2, J=2$) to d -orbitals, and ($j=3, J=3$) to f -orbitals (Table IV).

These SF projection operators access states in which the total angular momentum J is carried primarily by the molecule, i.e., there is no end-over-end angular momentum l . Since these projection operators depend only on the coordinates of the AB molecule in the SF frame, and not the coordinates of the X atom, they can be generalized without further modification to the analysis of angular excitations in larger clusters, $n > 1$, which are associated with states in which the total cluster angular momentum J is also associated with a “good” molecular angular momentum $j \approx J$. Thus there is no angular momentum in the atomic component, X_n , and also no relative angular momentum in these states. It is also possible to extend the MF projection operators to clusters with $n > 1$. However, for the $AB-X$ dimer, we shall see below that the exact eigenenergies for states dominated by $l=0$ can be obtained with equal ease from either representation. Analysis of the absorption spectrum for $AB-X$ will also show that the states accessed by the SF projectors give rise to the dominant transitions (Sec. IV). Therefore, we use the SF projectors for the larger clusters here.

D. POITSE excitation energies

We first present POITSE results for the $AB-X$ dimer. For $m_X = m_{\text{He}}$, we make comparison with the DVR-FBR calculations of Sec. II C. The effect of varying the mass m_X is then briefly analyzed, followed by the behavior for $n > 1$.

Optimized trial function parameters for ψ_T are given for $m_X = m_{\text{He}}$ in line 2 of Table III, together with the reference energy E_{ref} . All excitation energies are referred to the ground state energy of the total system, $E_0 = 449.97 \text{ cm}^{-1}$. (The ground state energy obtained in a separate DMC calculation agrees to within 0.01% with this DVR-FBR value.) The POITSE analysis is simplest for the intramolecular vibrational coordinate r , where behavior characteristic of a harmonic excitation is seen. Thus MC evaluation of the imaginary time correlation function for the projector $(r - r_e)$ followed by maximum entropy inversion yields an excitation spectrum consisting of a single sharp peak at energy $\omega = 981 \text{ cm}^{-1}$, in good agreement (3%) with the harmonic frequency value, $\omega_{\text{HO}} = 947.98 \text{ cm}^{-1}$ (Table I). The projector $(r - r_e)^2$ yields the first overtone, $\omega = 1920 \text{ cm}^{-1}$ ($\approx 2\omega_{\text{HO}}$) and a second peak at $\omega \approx 0 \text{ cm}^{-1}$, while $(r - r_e)^3$ yields the second overtone, $\omega = 2925 \text{ cm}^{-1}$ ($\approx 3\omega_{\text{HO}}$) and the harmonic frequency $\omega \approx \omega_{\text{HO}}$ as well.

Results from projection along the intermolecular stretching coordinate R are somewhat more complex, due to the strong anharmonic character of the potential along this coordinate. The DVR-FBR excitation energy corresponding to one vibrational quantum in R lies at $\omega = 22.87 \text{ cm}^{-1}$, very close to the dissociation limit. For anharmonic oscillators, all powers of the coordinate operator generally have nonvanishing off-diagonal matrix elements. We therefore cannot expect well resolved spectra with isolated peaks. Calculations with POITSE using projectors $(R - R_e)$ and $(R - R_e)^2$ both yield two peaks in this extremely difficult situation, one corresponding to the self-projection near zero and another one which can be assigned to the stretch excitation, but which is too broad to extract a reliable frequency.

The excitation energies derived from POITSE calculations with MF projectors for angular degrees of freedom are shown in the right hand section of Table II. For most of these projectors, the $\kappa(\omega)$ spectra consist of one single symmetric peak or two well separated symmetric peaks, where one of these can clearly be identified as the primary peak and the second one is much less intense. In those cases where the $\kappa(\omega)$ spectrum does not consist of well separated peaks, but the mean peak position can still be calculated, the POITSE excitation energy is given in parentheses. Comparison of the POITSE results with the DVR results listed in the left hand section of Table II shows an agreement between both calculations to within at least 6% for the good projectors, and in some instances to 1%. The probabilities $\mathcal{P}_{|k|j}^p$ in the left hand section provide a useful measure for the quality of the POITSE projection operator, with the empirical correlation that POITSE projection operators having $\mathcal{P}_{|k|j}^p > 0.75$ yield good results for excitations in this $AB-X$ ($m_X = m_{\text{He}}$) system. This can be used as a criterion for good projectors, albeit empirical and qualitative in nature. [The quality of the $\kappa(\omega)$ spectrum is not precisely quantifiable, depending on (i) the intensity of the main peak, given by $\mathcal{P}_{|k|j}^p$ if the total spectral intensity is normalized to one, (ii) the gap between the main and the less intense additional peaks, and (iii) the number of additional, but less intense peaks.]

The POITSE excitation energies derived from the SF projectors for $J=j$, $J=1, 2, 3$ ($l=0$) are listed in columns

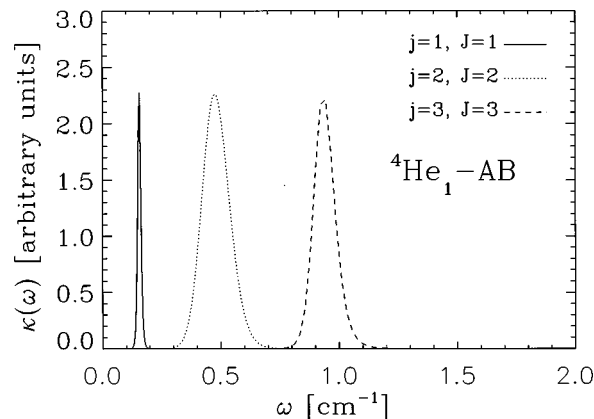


FIG. 4. POITSE excitation spectrum for $AB\text{-}^4\text{He}$, obtained with SF projectors, $l=0$, $J=j$ for $J=1, 2$, and 3 , respectively. Each $\kappa(\omega)$ spectrum shown is derived from one of the corresponding space-fixed projectors, using the trial wave function ψ_T . The excitation energies in Table IV are derived from the single intense and sharp peak in each case. Parameters for the reduced dimensionality model of $\text{SF}_6\text{-He}$ were used for $AB\text{-}^4\text{He}$.

three and four of Table IV, with the fourth column containing the M -averaged excitation energy, $\omega_{J,\text{ave}}$ and its associated standard deviation. Some of the projection operators are identical to MF projection operators (compare Table II), and for these we have therefore listed the corresponding exact excitation energy obtained by DVR-FBR in the last column, obtained by the same procedure of identification of maximal values of $\mathcal{P}_{|k|j}^p$.

Figure 4 shows three sample spectra $\kappa(\omega)$, obtained using one of each of the projectors for $j=1$, $j=2$, and $j=3$. Each spectrum shows one intense, sharp peak, indicating that these projectors are indeed projecting principally on one excited state. The ω_j values listed in Table IV are obtained from this intense peak. Two of the projectors for $j=3$ do not show well resolved single peaks but rather asymmetric, broadened peaks, and here we have not extracted excitation energies (entries “—” in Table IV).

Comparison of the M -averaged POITSE results with the exact excitation energies shows agreement within 7%. The differences between POITSE and exact values lie outside the statistical spread derived from the M -averaging. The differences could possibly be lowered by making longer POITSE runs and increasing the sampling. Nonstatistical error sources have been discussed in Ref. 5. Empirically, most of the SF projection operators summarized in Table IV are good, in the sense that they produce well-defined POITSE spectra consisting of δ -peaks with this level of sampling. In fact, with POITSE it appears not to be crucial in practice which representation for the projection operator is employed, provided that a reasonably “good” projector is used.

An example of less “good” projectors is provided by the SF projectors derived from Eq. (21) for $l \neq 0$ [Eq. (41)], not shown in Table IV. Analysis of the MC data for calculations using projectors corresponding to $l > 0$, $j=0$, showed that these are not good projectors, in the sense defined earlier in this section. This is reminiscent of the situation in case (b) coupling,⁴⁶ where j (angular momentum of the diatomic in the SF frame) may remain an approximately good quantum number, while l , the end-over-end angular momentum of the

TABLE V. POITSE results for excitations corresponding primarily to molecular rotation, obtained using SF projectors of Table IV. Upper section: $AB-X$ system with variable mass m_X . Lower section: $AB-X_n$ clusters, $n = 2, 3$. Energies $\omega_{J,\text{ave}}$, $J = 1, 2$ and 3 , are defined as averages over results from all projectors with the same J and with $l = 0$ (see text).

m_X	n	$\omega_{1,\text{ave}}$ [cm^{-1}]	$\omega_{2,\text{ave}}$ [cm^{-1}]	$\omega_{3,\text{ave}}$ [cm^{-1}]
$(3/4)m_{\text{He}}$	1	0.169	0.501	1.023
m_{He}	1	0.158	0.479	0.963
$2m_{\text{He}}$	1	0.144	0.462	0.894
$3m_{\text{He}}$	1	0.137	0.414	0.808
$4m_{\text{He}}$	1	0.122	0.371	0.742
$5m_{\text{He}}$	1	0.121	0.367	0.690
m_{He}	2	0.142	0.436	0.851
m_{He}	3	0.118	0.369	0.760

complex in the SF frame, is not conserved. It is consistent with the findings of the DVR-FBR calculations presented in Sec. II C.

Inspection of the $\mathcal{P}_{[K]j}^I$ values in Table II for those MF projectors identical to SF projectors of Table IV shows that not only are the latter “good” projectors in the sense of producing clean excitation spectra (Fig. 4), but also that the molecular angular quantum number j is a “good” quantum number for the corresponding excited states. This is generally true for the $AB-X$ dimer system. Table V shows the excitation energies $\omega_{J,\text{ave}}$ for $J = 1, 2$, and 3 as a function of the mass of atom X in the dimer. (Trial function parameters for all mass combinations are listed in Table III, together with the reference energies used.) All excitation energies $\omega_{J,\text{ave}}$ show a systematic decrease as m_X increases. This can readily be understood in terms of the increased moment of inertia associated with the overall rotation of the dimer as the mass increases (Sec. IV).

POITSE calculations with the SF projectors for $J = j$ were carried out for the larger clusters $AB-X_n$ using the trial wave function, Eq. (35), i.e., a product of dimer functions between AB and each X atom, and pair-wise correlation functions between the X atoms. For $m_X = m_{\text{He}}$, these calculations simulate the behavior in small clusters of ^4He , with the Bose statistics correctly incorporated via the permutation symmetry of ψ_T . The behavior of the $J = j$ excitations having no angular momentum in the helium component would then appear to be the most relevant ones to the behavior in a superfluid helium cluster. Since the corresponding SF projectors depend only on the molecular component, there are in principle no additional complications introduced when $n > 1$. The clusters $AB-X_n$ with $n = 2, 3$ require 12- and 15-dimensional POITSE calculations, respectively. The CPU requirements vary as approximately 1:1.7:2.7 for $n = 1:2:3$ (9:12:15 dimensions). More critical is the increase in statistical noise with dimensionality, which is an important factor in the maximum entropy analysis. Figure 5 compares the decay and associated standard deviations of $\tilde{\kappa}(t)$ for the 9-dimensional ($n = 1$) and 15-dimensional calculations ($n = 3$). Each decay curve is constructed from about 500–1000 independent calculations here. The noise increases with time⁵ and is also significantly larger for higher dimensional systems. Calculations for larger cluster sizes $n > 3$ are pos-

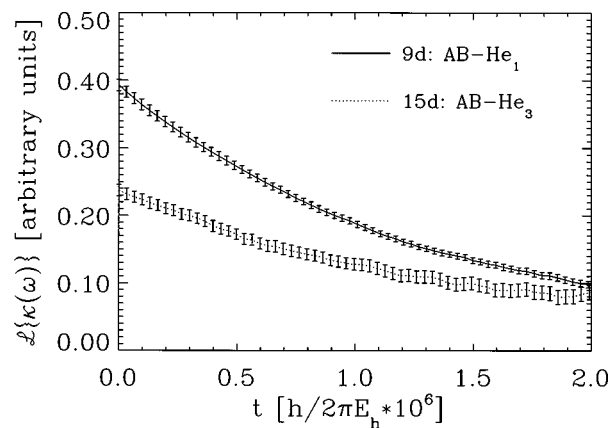


FIG. 5. $\tilde{\kappa}(t)$ as a function of imaginary time t for $AB-^4\text{He}_n$, $n = 1$ and 3 . The exponential decay for the 9-dimensional system $AB-^4\text{He}_1$ is shown in comparison with that for the 15-dimensional system $AB-^4\text{He}_3$. The statistical noise increases as a function of time, and is greater for higher dimensional systems.

sible, but would best be performed after a systematic analysis of the size scaling of the noise, and with a parallel version of the coded algorithm.

The resulting POITSE excitation energies $\omega_{J,\text{ave}}$, $J = 1, 2$ and 3 , for $n = 2$ and 3 are listed in the lower portion of Table V. Figure 6 shows $\kappa(\omega)$ for three projectors (compare to Fig. 4). As n increases, these also show a systematic decrease in $\omega_{J,\text{ave}}$, for a given J . The relation of this trend in rotational excitations for larger clusters to the more easily analyzed behavior of the dimer, is discussed below, together with its implications for spectra of molecules in $^4\text{He}_n$.

IV. TRANSITION INTENSITIES AND EMPIRICAL ENERGY LEVEL PATTERNS

The results in the previous sections show that when the molecule AB is attached to one or more helium atoms, there exist low lying excited states in which the molecular quantum number j remains a “good” quantum number and where this provides the major contribution to the total angular momentum J of the cluster. For the dimer this can be regarded as merely reflecting the fact that the molecular rotation is strongly coupled with the overall rotation of the complex, as

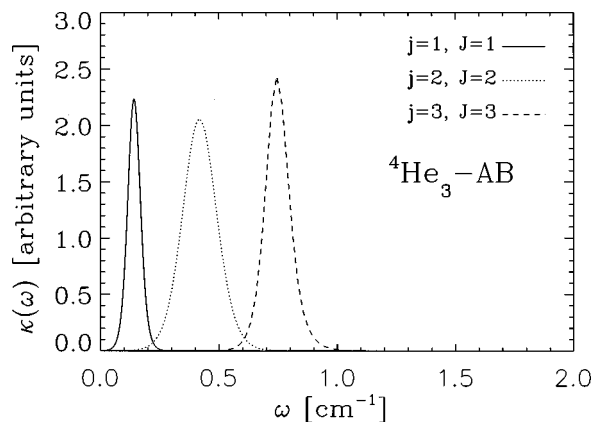


FIG. 6. POITSE excitation spectrum for $AB-^4\text{He}_3$ obtained with SF projectors. For details see caption to Fig. 4.

we discuss below. While these clusters are too small to be treated as liquid clusters possessing distinct interior and surface regions (and hence analogously distinct excitations), the helium component is nevertheless delocalized about the molecular species, as is well known from many ground state DMC studies.⁴⁷ In this section we now examine the relation between the energy levels calculated in Secs. II and III, and the molecular absorption spectrum. We begin with the AB - X dimer, for which the DVR-FBR calculation allows the complete rovibrational spectrum to be calculated. Transition energies between POITSE excited states for AB - X are assigned to spectral features with the help of this. We then analyze the corresponding transition energies for the larger clusters and discuss the behavior of these in connection with the experimental infrared spectra for SF_6 in 4He_n measured by Hartmann *et al.*¹¹

The DVR-FBR calculations for the AB - X ($m_X = m_{He}$) dimer system described in Sec. II produce all energy levels and associated eigenfunctions. Only a few of these were presented and analyzed in Sec. II C. In order to make contact with spectroscopic experiments, we need to determine which of the excited states receive dipole strength from the ground vibrational state manifold. Infrared absorption measurements on molecular chromophores in helium clusters show rotational fine structure accompanying vibrational transitions, at temperatures of 0.15–0.4 K. Thus we need to calculate the rovibrational line intensities for transitions from all rovibrational levels which are thermally populated at these temperatures. The spectral distribution is given by

$$\sum_{\alpha} \sum_{\alpha'} e^{-\beta E_{\alpha}} |\langle \alpha | \mu | \alpha' \rangle|^2 \delta(E_{\alpha'} - E_{\alpha} - \omega), \quad (42)$$

where μ is the dipole operator, and $\beta = 1/kT$. We assume the molecular transition dipole moment to lie along the AB axis \mathbf{r} and to be unmodified by the presence of the He, consistent with the very low polarizability of the latter. (For a strongly polar AB the effects of polarization may become significant.⁴⁸) The decoupling between the diatomic oscillator and both the van der Waals and overall rotation modes in our model potential (Sec. II A) then allows the rovibrational line intensities to be factorized into a diatomic factor $\mu_{v,v'}$, and an overlap between rovibrational wave functions. The latter can be constructed from direction cosine matrix elements together with the DVR-FBR eigenvectors. (According to our potential model, the vibrational part of any rovibrational eigenvector $|\alpha\rangle$ can be first factored into an r -dependent term and a term dependent upon R and θ . Combining this with a dipole transition moment along \mathbf{r} yields the above factorization of the rovibrational line intensities $|\langle \alpha | \mu | \alpha' \rangle|^2$.) These line intensities can then be interpreted as the rotational line strengths associated with a vibrational transition between levels v and v' of AB . They obey strict selection rules which are: $\Delta J = 0, \pm 1$, p alternates according to $0 \leftrightarrow 1$, and σ changes from $+$ to $-$ and vice versa. The dominant transitions are associated with $\Delta K = 0$, reflecting the near symmetric top character of the dimer complex.

Our reduced dimensionality model of SF_6 requires a formal modification here in order to allow simulation of these line strengths. The simplified model replaces SF_6 by a homo-

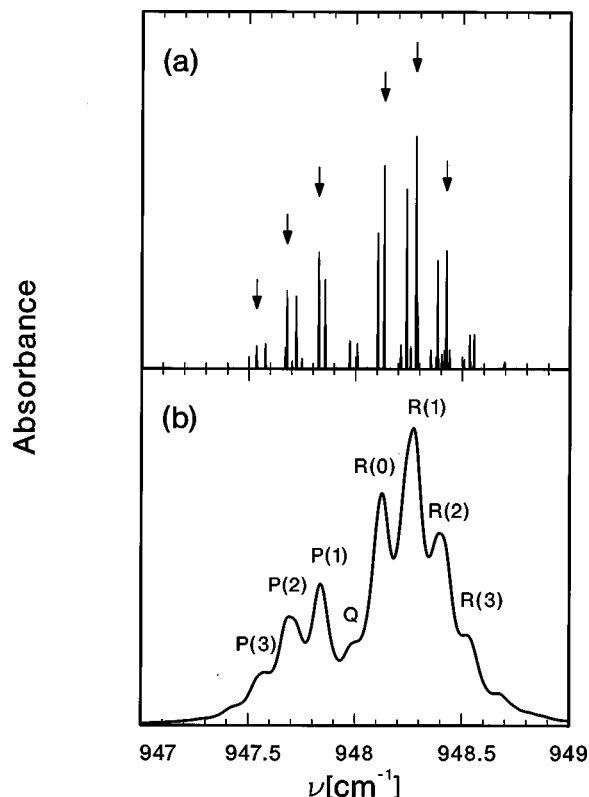


FIG. 7. (a) Stick spectrum from the DVR-FBR calculation for the AB - X model system with $m_X = m_{He}$, including levels up to $J = 6$ and assuming a dipole moment along the AB -axis (see text). Line strengths have been weighted by Boltzmann factors computed for a temperature of 0.4 K. Arrows show the transitions predicted from the POITSE excitations accessed by SF projectors with $J = j$. (b) Convolution of the stick spectrum with a Lorentzian line shape function with $FWHM = 0.085 \text{ cm}^{-1}$. The asymmetry splitting of the K -structure and the line doubling is now masked completely and only the P -, Q -, R -structure is visible.

nuclear diatomic, A_2 , with masses $m_A = 2m_F$. Like SF_6 , this model diatomic has no permanent dipole moment. However, while SF_6 has a nonzero transition dipole moment between the ground vibrational state and the triply degenerate ν_3 mode probed in the experiments of Hartmann *et al.*,¹¹ all dipole matrix elements of a homonuclear diatomic molecule are zero. Therefore we augment the reduced dimensionality model by adding a nonzero vibrational transition moment to emulate the properties of SF_6 and similar molecules. Note that since the vibrational transition moment appears only as a constant prefactor in all rotational line strengths, it does not affect the rotational fine structure and the band shape of interest here.

Figure 7(a) shows the thermally weighted line intensities obtained from all energy levels up to and including $J = 6$, at a temperature of 0.4 K, which corresponds to the temperature observed in experiments with large helium clusters, and which is also realistic for rotational temperatures of small van der Waals clusters. The transitions fall into groups which can be identified with the P -, Q -, and R -transitions of an asymmetric top near the prolate symmetric top limit. The doubling of lines is due to the presence of another set of transitions originating from the low lying first $\sigma = -$ state, which has a significant thermal occupation under these con-

ditions and a slightly denser rotational structure. These lines are well reproduced by the asymmetric top rotation constants A , B and C computed from the lowest $J=0$ and $J=1$ levels (Sec. II C). Because of the small asymmetry, a good fit to the first six rotational levels is also obtained with the effective symmetric top formula Eq. (28). The spectrum for $AB-X$ differs from that of the free diatom AB by the presence of a weak Q -branch, indicating a nonlinear rotor having energy levels with $K>0$ as a result of the He atom density located off-axis from AB . The low thermal occupation of higher J , and in particular higher K -levels, has a significant effect on the appearance of the spectrum. The deviations from a symmetric top spectrum become apparent at $K=4$ (see Fig. 3), which requires $J\geq 4$. At the chosen temperature of 0.4 K, the decreasing occupation numbers mask the increasing asymmetry splitting for $J\geq 4$ and preserve the appearance of a symmetric top spectrum. The asymmetry is masked even further if the infinite resolution stick spectrum is convoluted with a Lorentzian line shape. With a full width at half maximum (FWHM) width of 0.085 cm^{-1} , which gives the same line spacing/width ratio as seen in the experiments of Hartmann *et al.* for SF_6 in $^4\text{He}_n$,⁴⁹ one obtains a spectrum where only symmetric toplike J -structure with a thermally largely suppressed Q -branch survives [Fig. 7(b)]. In this situation it is very difficult to distinguish between a prolate symmetric rotor, an asymmetric rotor, or even a linear rotor.

The spectrum of the $AB-X$ ($m_X=m_{\text{He}}$) dimer is therefore characterized by the rotation of the complex as a whole, since the fitted symmetric top rotational constant is equal to the ground state rotational constant \bar{B} , Eq. (28). \bar{B} is necessarily smaller than the gas phase rotational constant of AB , B_0 , because the moment of inertia is higher. It is important to distinguish this overall rotation from the internal rotation states observed as higher excitations in the internal bending coordinate θ , for the nonrotating cluster with $J=0$ (Sec. II C). The energy spacing of these internal rotation states is characterized by an *increased* effective rotational constant, f , which has exactly the value predicted for the bending mode in Eq. (20) [see also Eq. (27) and the subsequent discussion].

For larger clusters we are not able to calculate the corresponding absorption spectrum, but we can make inferences from the POITSE results. Thus, the transition energies derived from the POITSE excitation energies with the SF projectors $J=j$ are shown in Fig. 7(a) by arrows. These can clearly be identified with the maximum intensity transitions in the $AB-X$ dimer. Figure 7 also shows that the POITSE transitions can clearly be taken as representative of the position of the corresponding rigid molecule assignment in a broadened spectrum. Since the transition dipole strength is carried by the molecule, it is therefore reasonable to presume that the corresponding excitations in larger clusters will also give rise to transitions with significant intensity. The energy differences between the POITSE excitation energies derived for $n>1$ therefore contain information about the corresponding absorption spectrum.

In particular, the energy level pattern of the SF-derived POITSE excitations can be fit to the free rotor model, Eq. (27), which applies to linear molecules as well as to a K

TABLE VI. Rotational constants derived from the POITSE energy calculations reported in Table V. B_F is calculated by fitting to the energy level pattern of a free rotor [$\omega_{J,\text{ave}}=B_F J(J+1)$], neglecting the centrifugal term (see text). The last column shows the ratio of B_F and the rotational constant $B_0=0.091\text{ cm}^{-1}$ of the free AB molecule.

m_X	n	$B_F [\text{cm}^{-1}]$	B_F/B_0
$(3/4)m_{\text{He}}$	1	0.085	0.93
m_{He}	1	0.080	0.88
$2m_{\text{He}}$	1	0.075	0.82
$3m_{\text{He}}$	1	0.068	0.75
$4m_{\text{He}}$	1	0.062	0.68
$5m_{\text{He}}$	1	0.058	0.64
m_{He}	2	0.071	0.78
m_{He}	3	0.063	0.69

$=0$ symmetric top. Since we only have three excited state energies, only the rigid rotor limit is reliable. Values of the resulting rotational constant $B_F [\omega_{J,\text{ave}}=B_F J(J+1)]$ for the reduced dimensionality $\text{SF}_6\text{-He}$ dimer, and for the variable m_X analogs are summarized in the top section of Table VI, and for the larger clusters, $n>1$ with $X\equiv^4\text{He}$, in the lower section. The rigid rotor expression provides a remarkably good fit to both the dimer and the $n>1$ energy levels, with a typical root mean square (rms) value of about $2-10\cdot 10^{-3}\text{ cm}^{-1}$.

For these small clusters these effective rotational constants B_F reflect simply the increasing moment of inertia which is caused by either the increased mass of the X-atom or by their increasing number. The interaction between the diatomic and the other atoms is sufficiently strong to lock the overall rotation to the rotation of the diatomic, such that $J=j$ to a very good approximation. Similar behavior is seen in recent fixed node calculations for the $J=j$ rotational states of SF_6 in $^4\text{He}_n$ for $n\leq 8$, made with full rotation-translation diffusion Monte Carlo.⁴¹ These fixed node excited state calculations show a saturation in the reduction of B_F at $n=8$, which corresponds to the filling of all octahedral sites on the SF_6 molecule. The present study does not go to large enough cluster sizes for an analogous complete filling of the preferred binding sites around AB in this reduced dimensionality model of SF_6 . Therefore we do not yet see any saturation in the reduction of B_F here. The implications of a saturation in the reduction in B_F with size will be discussed elsewhere.⁴¹

While the cluster sizes studied here are too small to make realistic inferences about the role of superfluidity in the experimental spectra of molecules in $^4\text{He}_n$, there is nevertheless an important feature which is consistent with the Bose liquid ground state character of the ^4He component. This is the finding that the spectroscopically relevant states are those with $J=j$, i.e., having no angular momentum in the helium (for the $AB-X$ dimer, $l=0$). This is consistent with the ground state Bose character of the surrounding helium environment, in which excitations with angular momentum are of high energy, and unlikely to be created. Generalized to larger clusters, this becomes the usual argument that there are no low lying excitations in the superfluid and hence our assignment of $J=j$ would appear to be valid for all sizes.

A second striking feature arises from the analysis of energy levels of the $AB-X$ dimer, where nearly free internal rotation was seen at high levels in the bending mode, while the lower levels are strongly hindered. Coupling between θ and R results in the rotational constant for this being raised, relative to the free molecule. Such an increase for an almost free internal rotation has been seen before in atom-molecule complexes.³⁶ In our SF_6 -He reduced dimensionality model, the hindrance at low bend quantum number is due to the high barrier, and a lower barrier in the θ direction could allow free internal rotation also at low energies. However, the key conclusion of relevance to the experimental results for SF_6 and other molecules in 4He_n , is that it is not this internal rotation in the dimer complex which evolves into the spectroscopically observed levels in larger clusters, but rather the overall rotation of the entire complex. The clusters studied here are small enough that they also rotate with the molecule. For larger sizes we expect mainly atoms in the range of the first radial density maximum to be strongly coupled to the diatomic, such that eventually the motion of a subsystem containing the molecular impurity and a few strongly coupled neighbors is the dominant chromophore in infrared excitation experiments. Consequently, the empirical moment of inertia should saturate at a certain value independent of the total cluster size.⁴¹

V. CONCLUSION

We have demonstrated the general applicability of our projection operator imaginary time spectral evolution, POITSE, technique to the calculation of excited states of weakly bound van der Waals type model systems of the type $AB-X_n$. These systems have been treated fully in up to 15 dimensions ($n=3$), which is well beyond the capabilities of conventional quantum methods for rovibrational problems. The accuracy of the calculations is satisfactory and can in principle be improved by increased Monte Carlo sampling. This would require a parallelization of the present code, which is conceptually straightforward due to the inherent independence of the random walks involved in the algorithm.

A primary goal of this paper was the study of the performance and selectivity of possible choices for the projection operators in identifying important excitations. In order to gain a detailed picture of the excited states, we performed variational DVR-FBR calculations of the rovibrational spectrum of the model system $AB-X$ ($m_X=m_{He}$) which allowed the unequivocal assignment of all excited states. The comparison of these results with the POITSE calculations allows the following observations to be made on the projectors:

- (i) Projectors constructed as functions of radial coordinates in a molecule fixed frame allow the selective extraction of vibrational modes with dominant stretching character, while projectors formulated as spherical harmonics of internal angles allow the identification of bending levels.
- (ii) Application of projectors associated with the orientation of the diatomic constituent relative to a space-fixed coordinate system, which implicitly assume that the angular momentum quantum number of the di-

atomic is a good quantum number for the system, produces excited rotational states of the entire system, $J \approx j$. Apparently the interaction strength between the diatomic and the attached atoms is sufficiently strong to lock the two rotational motions to each other. Consequently, the rotational level spacings decrease with increasing cluster size.

The present calculations are a first step toward the understanding of the phenomenon of rovibrational structures of molecules inside large liquid helium clusters which are reminiscent of free rotor spectra, albeit with modified rotational constants. Significantly reduced effective rotational constants have been extracted from rotationally resolved infrared laser spectra observed for molecules with small rotational constants like SF_6 ¹¹ and OCS ¹³ in 4He clusters at temperatures of 0.15–0.4 K, while molecules with rotational constants in the wave number range (e.g., HF) do not exhibit this phenomenon.⁴⁴ While the coarse J -structure visible in the form of P -, Q -, and R -branches is well resolved in 4He clusters, no rotational fine structure could be resolved in experiments with 3He clusters.¹³ This observation has been taken as evidence for free rotation inside a superfluid versus rotation inside a more or less classical fluid at the typical cluster temperatures of 0.15–0.4 K, in analogy to the famous Andronikashvili experiment.

While the experiments are above the superfluid temperature for 3He , and thus do not allow the ground state fermionic system to be probed, it would be of great interest to explore the consequences of the fermionic statistics on the structure and excitations of $AB-^3He_n$. The POITSE results obtained here for Bose 4He_n show that the important angular momentum carrying excitations are those with $J=j$, and with zero angular momentum in the surrounding helium. This is compatible with the ground state Bose character of the 4He , and thus raises very interesting questions for the corresponding energy spectrum in clusters of 3He_n .

ACKNOWLEDGMENTS

D. Blume acknowledges support from Deutscher Akademischer Austauschdienst (DAAD) through a Doktorandenstipendium. M. Mladenović is supported by Sonderforschungsbereich 357 of the Deutsche Forschungsgemeinschaft. K. B. Whaley acknowledges support from the National Science Foundation under NSF Grant No. CHE-9616615, and thanks the Alexander von Humboldt Foundation for a Senior Research Award. D.B. and M.L. thank J. P. Toennies for his continuing interest and support, and K.B.W. thanks J. P. Toennies for his hospitality at the Max-Planck Institut für Strömungsforschung during a sabbatical year 1996–97 in which this work was begun. Computer time was made available through grants from Höchstleistungsrechenzentrum Jülich, and the NSF Metacenter and NPACI programs.

¹P. J. Reynolds, D. M. Ceperley, B. J. Alder, and W. A. Lester, Jr., *J. Chem. Phys.* **77**, 5593 (1982).

²B. L. Hammond, W. A. Lester, Jr., and P. J. Reynolds, *Monte Carlo Methods in Ab Initio Quantum Chemistry* (World Scientific, Singapore, 1994).

³J. B. Anderson, in *Quantum Mechanical Electronic Structure Calculations*

- with *Chemical Accuracy I*, edited by S. R. Langhoff (Kluwer, Dordrecht, 1994).
- ⁴M. Jarrell and J. E. Gubernatis, *Phys. Rep.* **269**, 133 (1996).
 - ⁵D. Blume, M. Lewerenz, P. Niyaz, and K. B. Whaley, *Phys. Rev. E* **55**, 3664 (1997).
 - ⁶D. Blume, M. Lewerenz, and K. B. Whaley, *J. Chem. Phys.* **107**, 9067 (1997).
 - ⁷D. Blume, M. Lewerenz, and K. B. Whaley, *Math. Comput. Simul.* **47**, 135 (1998).
 - ⁸A. McNichols and T. Carrington, Jr., *Chem. Phys. Lett.* **202**, 464 (1993).
 - ⁹Q. Wu, D. H. Zhang, and J. Z. H. Zhang, *J. Chem. Phys.* **103**, 2548 (1995).
 - ¹⁰C. Leforestier, L. B. Braly, K. Liu, M. J. Elrod, and R. J. Saykally, *J. Chem. Phys.* **106**, 8527 (1997).
 - ¹¹M. Hartmann, R. E. Miller, J. P. Toennies, and A. Vilesov, *Phys. Rev. Lett.* **75**, 1566 (1995).
 - ¹²M. Hartmann, F. Mielke, J. P. Toennies, A. Vilesov, and G. Benedek, *Phys. Rev. Lett.* **76**, 4560 (1996).
 - ¹³S. Grebenev, J. P. Toennies, and A. F. Vilesov, *Science* **279**, 2083 (1998).
 - ¹⁴J. M. Hutson, *Advances in Molecular Vibrations and Collision Dynamics*, edited by J. M. Bowman and M. A. Ralner (JAI, Stamford, CT, 1991), Vol. 1A, p. 1.
 - ¹⁵J. M. Hutson and A. E. Thornley, *J. Phys. Chem.* **100**, 2505 (1994).
 - ¹⁶J. C. Light, in *Time-Dependent Quantum Molecular Dynamics*, edited by J. Boreckhove and L. Lathouwers, NATO ASI Series (Plenum, New York, 1992), Vol. 299, p. 185.
 - ¹⁷A. R. Cooper and J. M. Hutson, *J. Chem. Phys.* **98**, 5337 (1993).
 - ¹⁸A. Ernesti and J. M. Hutson, *Phys. Rev. A* **51**, 239 (1995).
 - ¹⁹D. J. Nesbitt, *Chem. Rev.* **88**, 843 (1988).
 - ²⁰R. E. Miller, *Science* **240**, 447 (1988).
 - ²¹R. J. Saykally, *Acc. Chem. Res.* **22**, 295 (1989).
 - ²²A. Heikal, L. Banares, D. H. Semmes, and A. H. Zewail, *Chem. Phys.* **157**, 231 (1991).
 - ²³A. McIlroy, R. Lascola, C. M. Lovejoy, and D. J. Nesbitt, *J. Phys. Chem.* **95**, 2636 (1991).
 - ²⁴J. T. Farrell, Jr., S. Davis, and D. J. Nesbitt, *J. Chem. Phys.* **103**, 2395 (1995).
 - ²⁵J. T. Farrell, Jr. and D. J. Nesbitt, *J. Chem. Phys.* **105**, 9421 (1996).
 - ²⁶K. Liu, J. D. Cruzan, and R. J. Saykally, *Science* **271**, 929 (1996).
 - ²⁷E. H. T. Olthof, A. van der Avoird, P. E. S. Wormer, K. Liu, and R. J. Saykally, *J. Chem. Phys.* **105**, 8051 (1996).
 - ²⁸R. T. Pack, E. Piper, G. A. Pfeffer, and J. P. Toennies, *J. Chem. Phys.* **80**, 4940 (1984).
 - ²⁹R. N. Barnett and K. B. Whaley, *J. Chem. Phys.* **99**, 9730 (1993).
 - ³⁰Y. Kwon, D. M. Ceperley, and K. B. Whaley, *J. Chem. Phys.* **104**, 2341 (1996).
 - ³¹B. Bobin, C. J. Bordé, J. Bordé, and C. Bréant, *J. Mol. Spectrosc.* **121**, 91 (1987).
 - ³²R. A. Aziz, F. R. W. McCourt, and C. C. K. Wong, *Mol. Phys.* **61**, 1487 (1987).
 - ³³S. Green, *J. Chem. Phys.* **64**, 3463 (1976).
 - ³⁴B. T. Sutcliffe and J. Tennyson, *Mol. Phys.* **58**, 1053 (1986).
 - ³⁵M. Mladenović and Z. Bačić, *J. Chem. Phys.* **93**, 3039 (1990).
 - ³⁶J. W. I. van Bladel, A. van der Avoird, and P. E. S. Wormer, *J. Chem. Phys.* **94**, 501 (1991).
 - ³⁷G. Herzberg, *Molecular Spectra and Molecular Structure* (Krieger Reprint Edition, Malabar, FL, 1991), Vol. II.
 - ³⁸H. W. Kroto, *Molecular Rotation Spectra* (Wiley, New York, 1975).
 - ³⁹M. Caffarel and D. M. Ceperley, *J. Chem. Phys.* **97**, 8415 (1992).
 - ⁴⁰D. Blume, Ph.D. thesis, Universität Göttingen, 1998.
 - ⁴¹E. Lee, D. Farrelly, and K. B. Whaley (submitted).
 - ⁴²M. Lewerenz, *J. Chem. Phys.* **104**, 1028 (1996).
 - ⁴³R. K. Bryan, *Eur. Biophys. J.* **18**, 165 (1990).
 - ⁴⁴D. Blume, M. Lewerenz, F. Huisken, and M. Kaloudis, *J. Chem. Phys.* **105**, 8666 (1996).
 - ⁴⁵R. P. Feynman, *Phys. Rev.* **94**, 2624 (1954).
 - ⁴⁶S. Bratož and M. L. Martin, *J. Chem. Phys.* **42**, 1051 (1965).
 - ⁴⁷K. B. Whaley, *Adv. Mol. Vibr. Collision Dyn.* **3**, 397 (1998).
 - ⁴⁸K. Higgins, F. M. Tao, and W. Klemperer, *J. Chem. Phys.* **109**, 3048 (1998).
 - ⁴⁹J. Harms, M. Hartmann, J. P. Toennies, A. F. Vilesov, and B. Sartakov, *J. Mol. Spectrosc.* **185**, 204 (1997).